Figure 4. Representative images of the Klüver-Barrera staining in the paramedian parts of the corpus callosum of the BCAS-operated mice treated with vehicle (A), vehicle+GW (B), Tel (Low; C), Tel (Low)+GW (D), Tel (High; E), and Tel (High)+GW (F) 30 days post-BCAS (n=7 each). Insets indicate enlarged images of oligodendrocytes. Histogram showing the grading of the white matter lesions of the 6 groups of mice (G–H; see Supplemental Method III for details). Representative images of immunohistochemistry for GST-π-positive oligodendrocytes in the medial parts of the corpus callosum of the BCAS-operated mice treated with vehicle (I) and Tel (Low; J) 30 days post-BCAS (n=7 each). Scale bar, 100 μm. Histogram showing the density of GST-π-positive oligodendrocytes (K) of the 2 groups of mice. Cerebral mRNA expressions of MCP-1 (L) and TNF-α (M) pre-BCAS and 30 days post-BCAS in the sham-operated or BCAS-operated mice treated with vehicle or Tel (Low; n=5 each). Tel (Low) indicates low-dose telmisartan (1 mg/kg per day); Tel (High), high-dose telmisartan (10 mg/kg per day); GW, GW9662 (1 mg/kg per day).
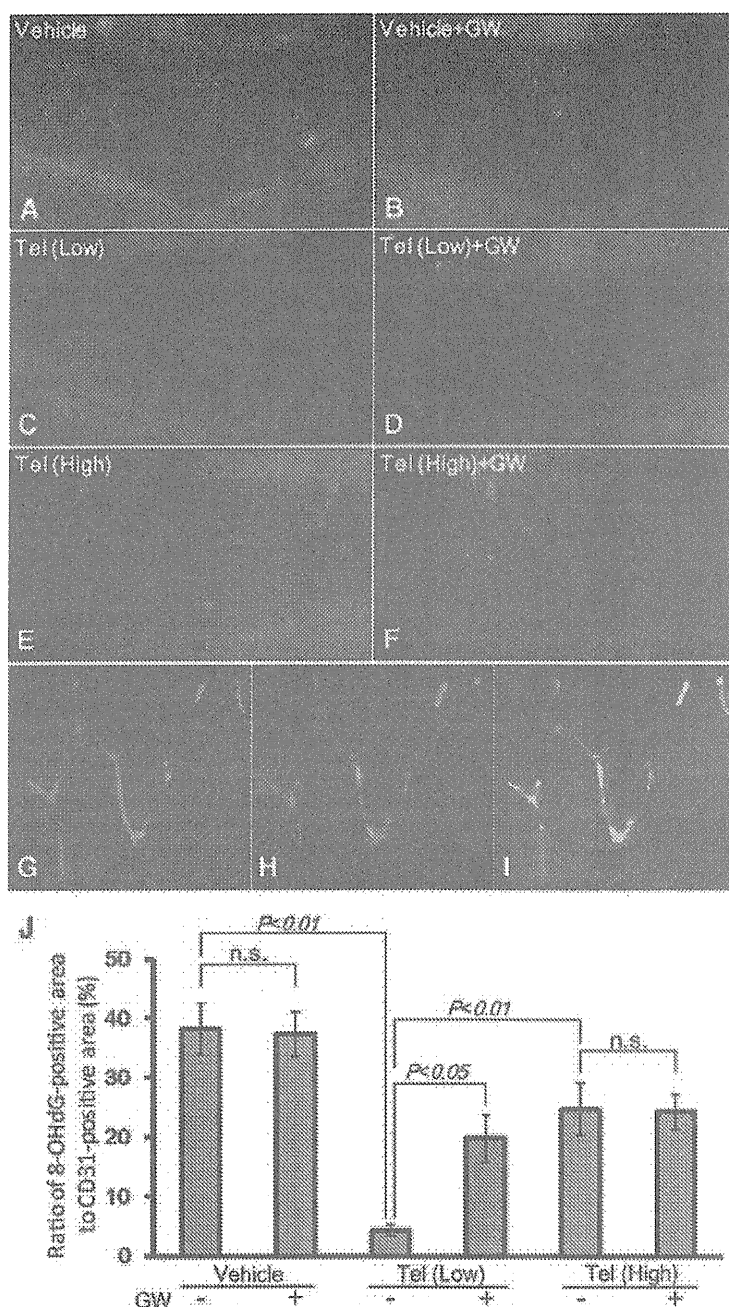
Figure 5. Representative images of the immunofluorescent staining for 8-OHdG (red) in the medial parts of the corpus callosum of the BCAS-operated mice treated with vehicle (A), vehicle+GW (B), Tel (Low; C), Tel (Low)+GW (D), Tel (High; E), and Tel (High)+GW (F) 30 days post-BCAS (n=7 each). Capillaries double-positive for CD31 (G, green) and 8-OHdG (H, red) and merged image (I) in vehicle-treated mice. Scale bars, 100 μm (A–F), 50 μm (G–I). Histogram showing the percentage of 8-OHdG-positive area to CD31-positive area of the 6 groups of mice (J). Tel (Low) indicates low-dose telmisartan (1 mg/kg per day); Tel (High), high-dose telmisartan (10 mg/kg per day); GW, GW9662 (1 mg/kg per day).

compare 5A, 5C, and 5E). Cotreatment with GW9662 did not lead to additional histological changes in mice with vehicle (Figure 5; compare 5A and 5B) or high-dose telmisartan (Figure 5; compare 5E and 5F).

Spatial Working Memory in Mice With Chronic Cerebral Hypoperfusion Was Restored by a Nonhypotensive Dose of Telmisartan

Finally, we analyzed spatial working memory of BCAS mice by the Y-maze test as the final functional output. The percentage of alternation behaviors significantly decreased in vehicle-treated BCAS mice compared with the sham-operated mice but significantly increased in a nonhypotensive dose of telmisartan-

treated mice. Such effects of low-dose telmisartan were partially offset by cotreatment with GW9662. Hypotensive doses of telmisartan-treated mice manifested in further impaired working memory (Figure 6A). There were no significant differences in the number of entries to each arm, which was considered to reflect locomotor activity, among the 5 groups (Figure 6B). These results suggest that a nonhypotensive dose of telmisartan, but not a hypotensive dose, improved spatial working memory of BCAS-operated mice.

Blood Concentration of Telmisartan

Plasma concentration after 1 mg/kg per day administration of telmisartan for 7 days was 142.86±14.85 ng/mL (n=4, values
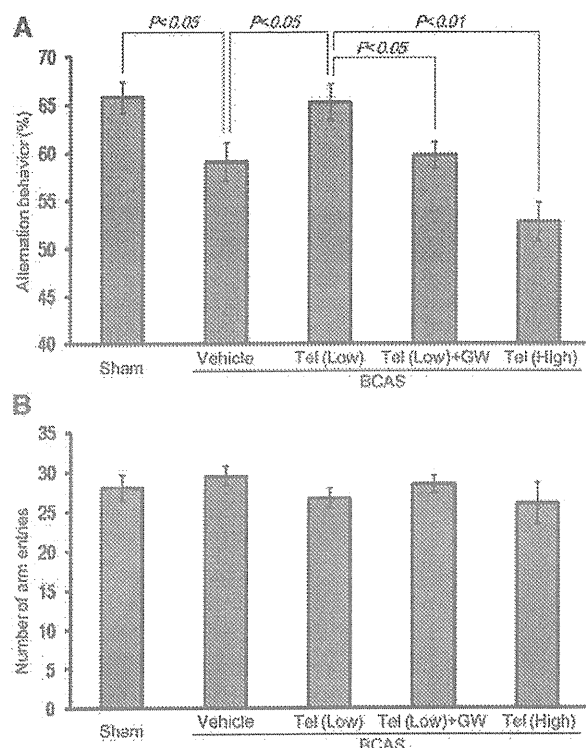
Figure 6. Spatial working memory assessed by the Y-maze test showing alternation behavior (%; A) and number of arm entries (B) of the indicated groups of mice (sham, vehicle+BCAS, Tel (Low)+BCAS, Tel (Low)+GW+BCAS; n=20, Tel (High) +BCAS; n=10). Tel (Low) indicates low-dose telmisartan (1 mg/kg per day); Tel (High), high-dose telmisartan (10 mg/kg per day); GW, GW9662 (1 mg/kg per day).

are expressed as mean±SEM), a lower limit of BP-lowering effect in humans.

Discussion

This study showed that (1) a nonhypotensive dose of telmisartan alleviated microglial/astroglial activation, endothelial oxidative stress, oligodendrocyte loss, and demyelinating changes in the white matter of the mice with chronic cerebral hypoperfusion; (2) such protective effects against the white matter lesions were at least partially mediated by anti-inflammatory and antioxidative effects that were exerted in part by PPAR-γ activation; (3) by contrast, a hypotensive dose of telmisartan did not induce such positive effects in BCAS-operated mice in the white matter; and (4) a nonhypotensive, but not a hypotensive, dose of telmisartan ameliorated cognitive decline of the BCAS-operated mice. Thus, the protective effects of telmisartan against white matter damage and cognitive impairment are exerted by its multifaceted effects, partially through PPAR-γ activation, but these are abolished by its BP-lowering effects when given at a higher dose. Thus, telmisartan should be considered for putative treatment for subcortical vascular dementia, although strict monitoring of BP is required.

Telmisartan is an ARB with a high degree of lipophilicity and is able to cross the blood–brain barrier. Telmisartan inhibits TNF-α-induced nuclear factor-κB activation, mainly

through AT$_1$ receptor blockade.[9] In addition, telmisartan suppresses MCP-1 expression through AT$_1$ receptor blockade and PPAR-γ activation.[10] Genetic deletion of AT$_1$ receptor protects against damage due to brain ischemia.[11] With its synergistic effects of AT$_1$ receptor blockade and PPAR-γ activation, telmisartan may exert multiple beneficial effects, including an antioxidative and anti-inflammatory effect, as shown in this study.

The nonhypotensive dose of telmisartan suppressed superoxide production from the vessel wall without lowering CBF. Telmisartan reduces NADPH oxidase activity[10]; therefore, administration of telmisartan in such a low dose seems to decelerate the free radical system in the chronically hypoperfused mouse brain. However, a hypotensive dose of telmisartan substantially increased the degree of endothelial oxidative stress together with glial activation, white matter lesions, and spatial working memory deficits. Because mice with severe CBF reduction (approximately lower than 50% of the baseline level) died and were subsequently excluded from the analysis, such detrimental effects of high-dose telmisartan may even be underestimated. ARBs protect against ischemic cerebral injury, independently of BP.[12] The benefit of normotension over hypotension lies in the absence of hypotension-induced aggravation of ischemic change. In the PRoFESS study, lowering BP at the subacute phase after stroke (within 15 days) may have decreased CBF. The Acute Candesartan Cilexetil Therapy in Stroke Survivors (ACCESS) study indicated that candesartan treatment immediately after stroke, without significant lowering of BP, decreased the rate of recurrent stroke.[13] Therefore, the beneficial pleiotropic effect of telmisartan seems to be overwhelmed by BP-lowering if given in a high dose. Caution should therefore be exercised when lowering BP at an acute to subacute stage when cerebrovascular autoregulation is damaged. In clinical practice, appropriate timing and dose of telmisartan should be considered.

The effect of telmisartan on cognitive function was also assessed. The Y-maze tests showed that spatial working memory was significantly disrupted by chronic cerebral hypoperfusion. Nonhypotensive doses of telmisartan significantly attenuated the deterioration of spatial working memory together with histological improvement in the white matter. By contrast, hypotensive doses of telmisartan further aggravated spatial working memory together with histological deterioration. In this mouse model, pathological changes were restricted in the white matter only. The cerebral cortex and hippocampus, which are associated with spatial working memory,[14] were not damaged in a relatively short period (for example, 30 days post-BCAS). Thus, telmisartan may have restored frontal–subcortical circuitry function, which is also associated with spatial working memory.[8,14] However, hippocampal changes appear at 3 months post-BCAS[15]; it would therefore be of interest to extend the observation period to investigate effect of telmisartan on the gray matter in a future study.

Recently, it has been shown that cerebral endothelial cells secrete trophic factors that support the survival and proliferation of oligodendrocyte precursor cells.[16] Such oligodendrocyte precursor cell-supportive phenomena in endothelial cells are mediated by Akt and Src signaling pathways. Noncytotoxic levels of oxidative stress downregulate the production

of trophic factors such as brain-derived neurotrophic factor and fibroblast growth factor and disrupt the ability of cerebral endothelial cells to support oligodendrocyte precursor cells. Furthermore, GST-π-positive oligodendrocytes were restored by low-dose telmisartan. These data suggest that a novel function of telmisartan is to maintain "oligovascular niche" by sustaining oligodendrocyte homeostasis in mammalian brain.

In conclusion, long-term AT$_1$ receptor blockade and PPAR-γ activation with telmisartan should be considered as a novel therapeutic approach for protection from damage associated with chronic cerebral hypoperfusion or subcortical vascular dementia.

Disclosures

None.

References

1. Tzourio C, Anderson C, Chapman N, Woodward M, Neal B, MacMahon S, Chalmers J; PROGRESS Collaborative Group. Effects of blood pressure lowering with perindopril and indapamide therapy on dementia and cognitive decline in patients with cerebrovascular disease. *Arch Intern Med.* 2003;163:1069–1075.
2. Saxby BK, Harrington F, Wesnes KA, McKeith IG, Ford GA. Candesartan and cognitive decline in older patients with hypertension: a substudy of the SCOPE trial. *Neurology.* 2008;70:1858–1866.
3. Li NC, Lee A, Whitmer RA, Kivipelto M, Lawler E, Kazis LE, Wolozin B. Use of angiotensin receptor blockers and risk of dementia in a predominantly male population: prospective cohort analysis. *BMJ.* 2010;340:b5465.
4. Diener HC, Sacco RL, Yusuf S, Cotton D, Ounpuu S, Lawton WA, Palesch Y, Martin RH, Albers GW, Bath P, Bornstein N, Chan BP, Chen ST, Cunha L, Dahlöf B, De Keyser J, Donnan GA, Estol C, Gorelick P, Gu V, Hermansson K, Hilbrich L, Kaste M, Lu C, Machnig T, Pais P, Roberts R, Skvortsova V, Teal P, Toni D, VanderMaelen C, Voigt T, Weber M, Yoon BW; Prevention Regimen for Effectively Avoiding Second Strokes (PRoFESS) study group. Effects of aspirin plus extended-release dipyridamole versus clopidogrel and telmisartan on disability and cognitive function after recurrent stroke in patients with ischaemic stroke in the Prevention Regimen for Effectively Avoiding Second Stroke (PRoFESS) trial: a double-blind, active and placebo-controlled study. *Lancet Neurol.* 2008;7:875–884.
5. Benson SC, Pershadsingh HA, Ho CI, Chittiboyina A, Desai P, Pravenec M, Qi N, Wang J, Avery MA, Kurtz TW. Identification of telmisartan as a unique angiotensin II receptor antagonist with selective PPARγ-modulating activity. *Hypertension.* 2004;43:993–1002.
6. Tsukuda K, Mogi M, Iwanami J, Min LJ, Sakata A, Jing F, Iwai M, Horiuchi M. Cognitive deficit in amyloid-β-injected mice was improved by pretreatment with a low dose of telmisartan partly because of peroxisome proliferator-activated receptor-γ activation. *Hypertension.* 2009; 54:782–787.
7. Shibata M, Ohtani R, Ihara M, Tomimoto H. White matter lesions and glial activation in a novel mouse model of chronic cerebral hypoperfusion. *Stroke.* 2004;35:2598–2603.
8. Shibata M, Yamasaki N, Miyakawa T, Kalaria RN, Fujita Y, Ohtani R, Ihara M, Takahashi R, Tomimoto H. Selective impairment of working memory in a mouse model of chronic cerebral hypoperfusion. *Stroke.* 2007;38:2826–2832.
9. Nakano A, Hattori Y, Aoki C, Jojima T, Kasai K. Telmisartan inhibits cytokine-induced nuclear factor-κB activation independently of the peroxisome proliferator-activated receptor-γ. *Hypertens Res.* 2009;32: 765–769.
10. Matsui T, Yamagishi S, Ueda S, Nakamura K, Imaizumi T, Takeuchi M, Inoue H. Telmisartan, an angiotensin II type 1 receptor blocker, inhibits advanced glycation end-product (AGE)-induced monocyte chemoattractant protein-1 expression in mesangial cells through downregulation of receptor for AGEs via peroxisome proliferator-activated receptor-γ activation. *J Int Med Res.* 2007;35:482–489.
11. Walther T, Olah L, Harms C, Maul B, Bader M, Hörtnagl H, Schultheiss HP, Mies G. Ischemic injury in experimental stroke depends on angiotensin II. *FASEB J.* 2002;16:169–176.
12. Takizawa S, Dan T, Uesugi T, Nagata E, Takagi S, van Ypersele de Strihou C, Miyata T. A sartan derivative with a very low angiotensin II receptor affinity ameliorates ischemic cerebral damage. *J Cereb Blood Flow Metab.* 2009;29:1665–1672.
13. Schrader J, Lüders S, Kulschewski A, Berger J, Zidek W, Treib J, Einhäupl K, Diener HC, Dominiak P; Acute Candesartan Cilexetil Therapy in Stroke Survivors Study Group. The ACCESS Study: evaluation of acute candesartan cilexetil therapy in stroke survivors. *Stroke.* 2003;34:1699–1703.
14. Sarti C, Pantoni L, Bartolini L, Inzitari D. Persistent impairment of gait performances and working memory after bilateral common carotid artery occlusion in the adult Wistar rat. *Behav Brain Res.* 2002;136:13–20.
15. Nishio K, Ihara M, Yamasaki N, Kalaria RN, Maki T, Fujita Y, Ito H, Oishi N, Fukuyama H, Miyakawa T, Takahashi R, Tomimoto H. A mouse model characterizing features of vascular dementia with hippocampal atrophy. *Stroke.* 2010;41:1278–1284.
16. Arai K, Lo EH. An oligovascular niche: cerebral endothelial cells promote the survival and proliferation of oligodendrocyte precursor cells. *J Neurosci.* 2009;29:4351–4355.

Proteasome inhibition in medaka brain induces the features of Parkinson's disease

Hideaki Matsui,*† Hidefumi Ito,* Yoshihito Taniguchi,†‡ Haruhisa Inoue,*†[1] Shunichi Takeda†‡ and Ryosuke Takahashi*†

*Department of Neurology, Kyoto University, Graduate School of Medicine, Kyoto, Japan

†Core Research for Evolutional Science and Technology (CREST), Japan Science and Technology Agency, Kawaguchi, Japan

‡Department of Radiation Genetics, Kyoto University, Graduate School of Medicine, Kyoto, Japan

Abstract

Recent findings suggest that a defect in the ubiquitin-proteasome system plays an important role in the pathogenesis of Parkinson's disease (PD). A previous report (McNaught et al. 2004) demonstrated that rats systemically injected with proteasome inhibitors exhibited PD-like clinical symptoms and pathology. However, because these findings have not been consistently replicated, this model is not commonly used to study PD. We used medaka fish to test the effect of systemic administration of proteasome inhibitors because of the high level of accessibility of the cerebrospinal fluid in fish. We injected lactacystin or epoxomicin into the CSF of medaka. With proteasome inhibition in the medaka brain, selective dopaminergic and noradrenergic cell loss was observed. Further-more, treated fish exhibited reduced spontaneous movement. Treatment with proteasome inhibitors also induced the formation of inclusion bodies resembling Lewy bodies, which are characteristic of PD. Treatment with 6-OHDA also induced dopaminergic cell loss but did not produce inclusion bodies. These findings in medaka are consistent with previous results reporting that non-selective proteasome inhibition replicates the cardinal features of PD: locomotor dysfunction, selective dopaminergic cell loss, and inclusion body formation.

Keywords: dopamine, hydroxylase, medaka (*Oryzias latipes*), Parkinson's disease, proteasome inhibitor, tyrosine inclusion body.

J. Neurochem. (2010) 115, 178-187.

Parkinson's disease (PD) is characterized by the degeneration of dopaminergic and noradrenergic neurons in neuronal populations located primarily in the substantia nigra pars compacta and the locus coeruleus. Another symptom of PD is the presence of abnormal protein-rich structures known as Lewy bodies and pale bodies in the cytoplasm of neurons in the brainstem or cerebral cortex. Several lines of evidence show that defects in the ubiquitin-proteasome system may play an important role in the pathology of PD (Dawson and Dawson 2003). Mutations in the components of the ubiquitin-proteasome system such as parkin and ubiquitin C-terminal hydrolase L1 are responsible for a subgroup of familial PD (Kitada et al. 1998; Leroy et al. 1998). Impairment of the ubiquitin-proteasome system has also been implicated in idiopathic PD. For example, a decrement in proteasome activity or a decrease in subunits of the 20S proteasome and the PA700/19S complex was detected in the substantia nigra of PD patients (Tofaris et al. 2003; McNaught et al. 2006b; Cook and Petrucelli 2009).

Previously, it was reported that systemic exposure to proteasome inhibitors induced dopaminergic neuronal death and the formation of inclusion bodies similar to Lewy bodies (McNaught et al. 2004). Although this report widely attracted attention and some groups replicated the original results (Nair et al. 2006; Schapira et al. 2006; Zeng et al.

2006), the findings have not been consistently reproduced (Bové *et al.* 2006; Kordower *et al.* 2006; Manning-Boğ *et al.* 2006). The reason for this is unknown, but the authors of the original paper proposed several possibilities, including variation in the brain bioavailability of the toxin (McNaught and Olanow 2006a). To date, the proteasome inhibitors model of PD is not widely accepted as a useful model system for the study of PD (Beal and Lang 2006).

We previously generated genetic and toxin-induced models of PD using a small laboratory fish, medaka (*Oryzias latipes*) (Matsui *et al.* 2009, 2010). In this study, we report a method for the administration of various drugs and toxins into the CSF of medaka. Although we administered proteasome inhibitors and 6-hydroxydopamine (6-OHDA) non-selectively into medaka CSF using this new method, a selective loss of dopaminergic and noradrenergic neurons was induced. Inclusion bodies were observed 3 days after the administration of proteasome inhibitors. This medaka model replicates key features of PD: locomotor dysfunction, inclusion body formation and selective loss of dopamine and noradrenaline neurons.

Materials and methods

Proteasome inhibitors and 6-OHDA treatment

Wild-type medaka of the *Kyoto-cab* strain was used for this study. Medaka at 10 months post-fertilization were anesthetized with chloretone at a dosage of 0.35 μg/mL (Tokyo Chemical Industry, Tokyo, Japan). After sufficient anesthesia, each fish was moved into an agarose-gel plate with a dent filled with water (Fig. 1a). Each fish was gently grasped at the belly with the examiner's fingers and injected with toxins or non-toxic vehicles at a dosage of 0.8 μL/ 0.1 g body weight. The concentrations of toxins were as follows: 2 mM for lactacystin, 10 mM for 6-OHDA and 0.2 mM for epoxomicin. The vehicle for lactacystin and 6-OHDA is water and that for epoxomicin is dimethylsulfoxide. The mean volume (standard error) of injection is 1.52 (0.0045), 1.52 (0.0044), 1.52 (0.0045) μL for vehicle (water), lactacystin and 6-OHDA respectively, and 1.52 (0.0044), 1.52 (0.0045) μL for vehicle (dimethyl-sulfoxide) and epoxomicin respectively. Injections were made manually (about 1 s/injection) using a glass micropipette (GD-1; Narishige, Tokyo, Japan) attached to a Hamilton syringe (Hamilton, Reno, NV). The tip of the glass micropipette was positioned in the CSF space between the hindbrain and the optic tectum (Fig. 1b). The injection procedures can be seen in the Movie S1.

Proteasome activity assay

Each brain was homogenized in 200 μL ice-chilled buffer containing 20 mM Tris–HCl pH7.6, 1 mM EDTA, 1 mM dithiothreitol and 0.1% NP40. Homogenates were centrifuged at 14 000 g for 5 min at 4°C. The supernatants were used for determination of proteasome activity. Fifty micrograms of protein in 200 μL buffer was incubated with 10 μM Z-Leu-Leu-Glu-AMC (amido-methylcoumarin; Sigma Aldrich, St Louis, MO, USA) for 60 min at 37°C. For the negative control, we added 20 μM epoxomicin in the reaction buffer using vehicle-treated brains. The released AMC was detected at 1 min intervals by fluorescence at 460 nm (emission 355 nm) (Fluoroskan Ascent FL; Thermo Fischer, Waltham, MA, USA).

Western blotting

Brains were homogenized in RIPA buffer (25 mM Tris–HCl pH 7.6, 150 mM NaCl, 1% NP40, 1% sodium deoxycholate, 0.1% sodium dodecyl sulfate) with protease inhibitors and processed for sodium dodecyl sulfate–polyacrylamide gel electrophoresis. Immunoreactive bands were detected with ECL reagent or ECL plus reagent (GE Healthcare Life Sciences, Buckinghamshire, UK) and the chemiluminescent signal was visualized by exposing the membrane to Fuji RX-U X-ray film (Fuji Film, Tokyo, Japan). Films were scanned and densitometric analysis of blots was performed using ImageJ software (National Institutes of Health; http://rsbweb.nih.gov/ij/). The background intensity of the film was subtracted from the band intensity. A monoclonal antibody against tyrosine hydroxylase (TH) (1 : 1000, mouse monoclonal; Millipore, Billerica, MA, USA) and an anti-tryptophan hydroxylase antibody (1 : 1000, sheep polyclonal; Abcam, Cambridge, MA, USA) were used for the western blotting analysis of TH and tryptophan hydroxylase, respectively. For the detection of ubiquitin, an anti-ubiquitin antibody (1 : 1000, rabbit polyclonal; Dako, Glostrup, Denmark) was used. An anti-β-actin antibody (1 : 5000, mouse monoclonal, AC-15; Sigma-Aldrich, St Louis, MO, USA) was used for the loading control.
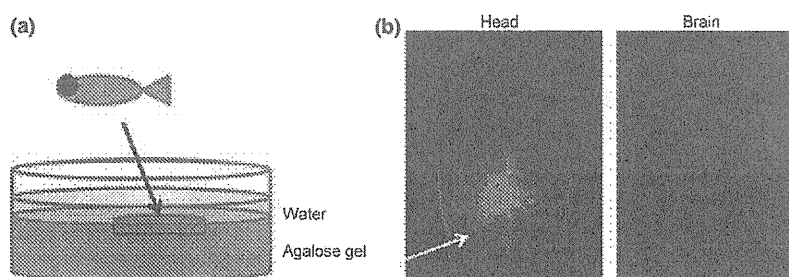

Fig. 1 Method of injection. (a) Simple illustration of the agarose bed for injection. The dent made it easy to hold the fish stationary. (b) Injected dye in the cerebrospinal fluid space. Images were taken by BIOREVO, BZ-9000 microscope (Keyence, Osaka, Japan). White arrow indicates the route for injection needle. The images were taken from above, soon after the injection of Alexa Fluor 546 (Invitrogen, Carlsbad, CA, USA). The left image is the photograph of the whole head and the right is that of the brain (after removal of the skull and other adjacent structures).

Immunohistochemistry

Immunohistochemistry was performed as previously described with minor modifications (Matsui et al. 2009, 2010). Each brain was sectioned at a thickness of 20 μm and sections were incubated with mouse anti-TH antibody (1 : 500, mouse monoclonal; Millipore) for 1 h. Immunoperoxidase detection was carried out using a Vector Elite ABC kit with 3,3'-diaminobenzidine (Vector Laboratories, Burlingame, CA, USA). Densitometric analysis of the striatum TH-positive fibers was performed by Photoshop software (Adobe, San Jose, CA, USA). Several sections were then counter-stained for Nissl substance. For staining of ubiquitin and synuclein, each brain was sectioned at 10 μm and an anti-ubiquitin antibody (1 : 100 for fluorescence, 1 : 500 for 3,3'-diaminobenzidine staining, rabbit polyclonal; Dako) and an anti-synuclein antibody (1 : 100, rabbit polyclonal, AB5464; Millipore) were used, respectively.

To determine the numbers of Nissl-stained cells, we selected the central section from the group of sections containing the middle diencephalic TH-positive cell cluster (when the section number was even, we chose the rostral section). We counted Nissl-stained cells in the optic tectum 300–400 μm lateral from the midline.

The staining specificity was assessed by replacing the primary antibodies with the appropriate amount of phosphate-buffered saline (PBS) solution containing 2% bovine serum albumin or by pre-incubating the primary antibodies with an excess of their respective

antigen. No reaction-product deposits were seen in the sections thus treated.

Transmission electron microscopy

For electron microscopic analysis, medaka brains were fixed overnight in 2% glutaraldehyde with phosphate buffer. After rinsing in 0.1 M PBS with 0.1 M sucrose, samples were post-fixed in 1% osmium tetroxide (OsO_4) with 0.1 M PBS and 0.1 M sucrose for 1.5 h. Samples were rinsed, dehydrated in an ethanol series, and embedded in Epon. The 80-nm thin sections were cut on an ultramicrotome. Sections were stained with uranyl acetate and lead citrate.

Behavioral analysis

Behavioral analysis was performed as previously described with slight modification (Matsui et al. 2009, 2010). Image acquisition began 5 min after the medaka was placed in a new water tank. Data were collected continuously for the subsequent 5 min.

Statistical analysis

Data were expressed as mean ± standard errors of the mean (SEM). An analysis of variance (ANOVA) was used to test results for statistical significance. Post hoc analysis using Bonferroni correction for multiple tests was used. Differences were considered significant when $p < 0.05$.
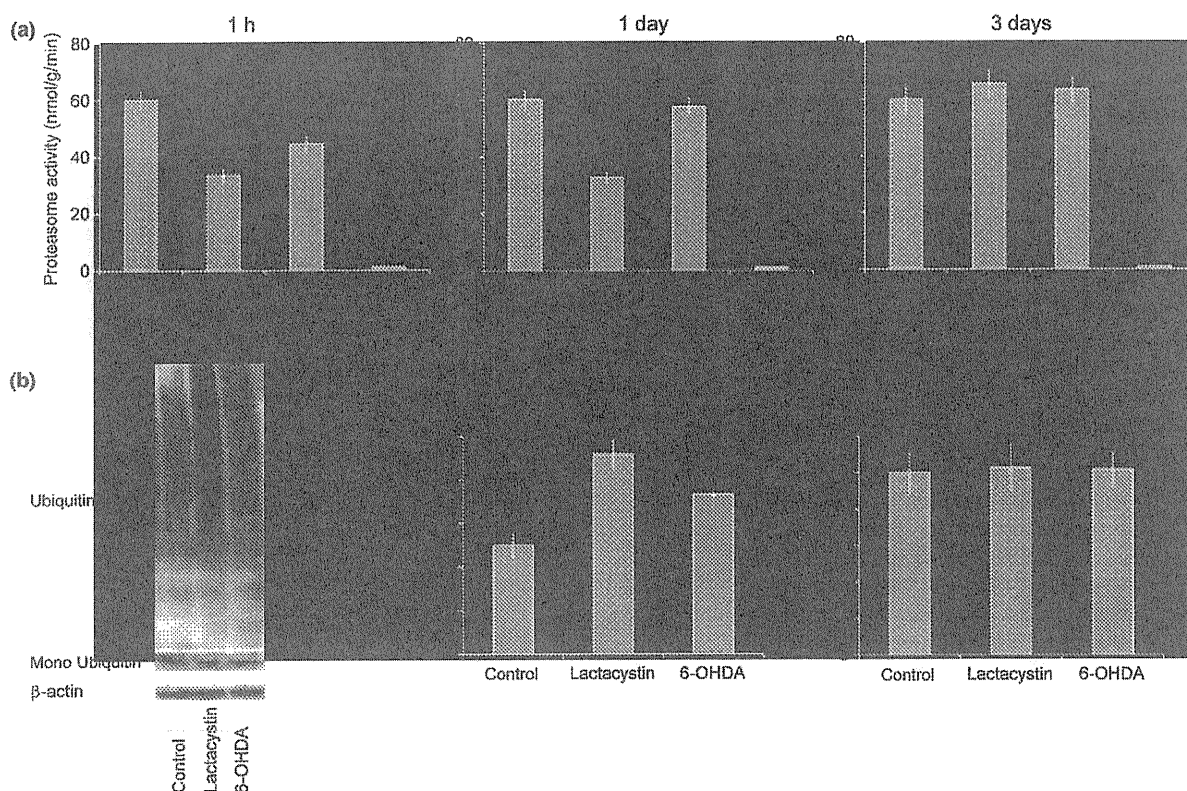

Fig. 2 Proteasome activity and the amount of ubiquitinated proteins of vehicle-, lactacystin- and 6-OHDA-treated medaka brain. (a) The upper and lower graphs show the proteasome activity 1 h and 3 days after injection, respectively ($n = 8$). (b) Ubiquitinated proteins of the whole brain (3 days after injection). β-Actin is for the loading control. The graph indicates the densitometric analysis of ubiquitin/β-actin and monoubiquitin/β-actin band ($n = 8$). $*p < 0.05$; $***p < 0.001$.

Results

Successful administration of materials into CSF of medaka

Using a glass micropipette coupled to a Hamilton syringe, various toxins and drugs were successfully delivered to medaka via the CSF. To verify drug delivery into the CSF but not in the brain parenchyma, we injected a fluorescent dye as a marker. Soon after injection, fluorescence was visible in the CSF space. After removal of the skull and adjacent structures, the signal totally disappeared, indicating that the dye did not enter the brain parenchyma (Fig. 1b). This method of drug delivery was used for all of the following experiments.

Reduced proteasome activity and increased ubiquitinated proteins in medaka treated with lactacystin

Proteasome activity was measured in the whole brain of normal, untreated medaka to determine baseline levels of proteasome activity (Fig. 2a) and compared with proteasome activity measured in medaka at different time-points following injection of the proteasome inhibitor lactacystin and the neurotoxin 6-OHDA. Each brain was intensively washed by PBS before the homogenization to avoid the carry-over of injected materials. The fluorescence signals increased linearly for the entire 60 min assay (data not shown). Addition of epoxomicin, a specific proteasome inhibitor, into the reaction buffer perfectly inhibited the fluorescence signals indicating this assay indeed reflected the proteasome activity. One hour after lactacystin injection, the proteasome activity in medaka brain was markedly decreased from baseline levels. 6-OHDA-treated medaka brain also showed mild reduction of proteasome activity. Three days after injection, the proteasome activity of lactacystin-treated and 6-OHDA-treated medaka brain became comparable to that of control brains (Fig. 2a).

Next, we compared the amount of ubiquitinated proteins in vehicle- and lactacystin-treated medaka using western blotting. Because medaka ubiquitin amino acid sequence is
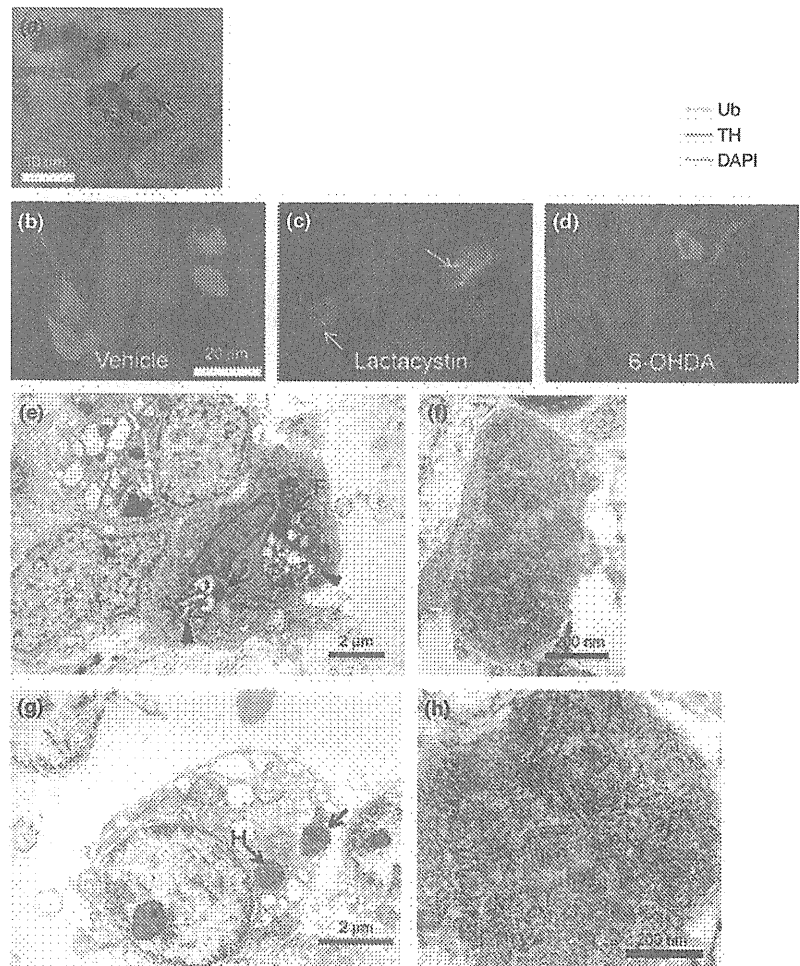

Fig. 3 Images of inclusions of lactacystin-treated medaka brain. (a) Lactacystin-treated, 3,3'-diaminobenzidine (DAB) staining (anti-ubiquitin antibody). Arrows indicate ubiquitin-positive inclusions. (b-d) Immunofluorescence staining with anti-ubiquitin, anti-TH antibody and DAPI. (b) Vehicle-treated. (c) Lactacystin-treated. White arrows indicate ubiquitin, TH-double positive inclusions. (d) 6-OHDA-treated. (e-h) Electron microscopic photographs of lactacystin-treated medaka brain. Black arrows indicate the inclusions and arrow heads indicate the lysosome. (e, g) Some inclusions were seen adjacent to the nucleus. (f, h) Enlarged image of (e) and (g).

identical to human sequence, we used commercially available anti-ubiquitin antibody (rabbit polyclonal; Dako). Three days after lactacystin injection, high molecular weight ubiquitin-positive bands increased in lactacystin-treated medaka brains compared with levels in controls. 6-OHDA-treated medaka brain showed a more modest increase of ubiquitinated proteins. The amount of mono ubiquitin did not differ among the groups (Fig. 2b).

These findings suggest that injection of lactacystin inhibited proteasome activity in medaka brain, resulting in an increase in ubiquitinated proteins.

Inclusion bodies seen in lactacystin-treated medaka

To test whether treatment with lactacystin resulted in an increase in inclusion bodies in medaka brain, we stained brain sections with an anti-ubiquitin antibody. Three days after injection of lactacystin, ubiquitin-positive cytoplasmic inclusions were seen in various regions of the brain (Fig. 3a). These inclusions were distributed throughout the brain, including the forebrain, optic tectum, diencephalon, hindbrain and spinal cord (data not shown). Some inclusions look like Lewy bodies, which are known to accompany PD (Fig. 3a). TH-positive neurons also contained inclusions
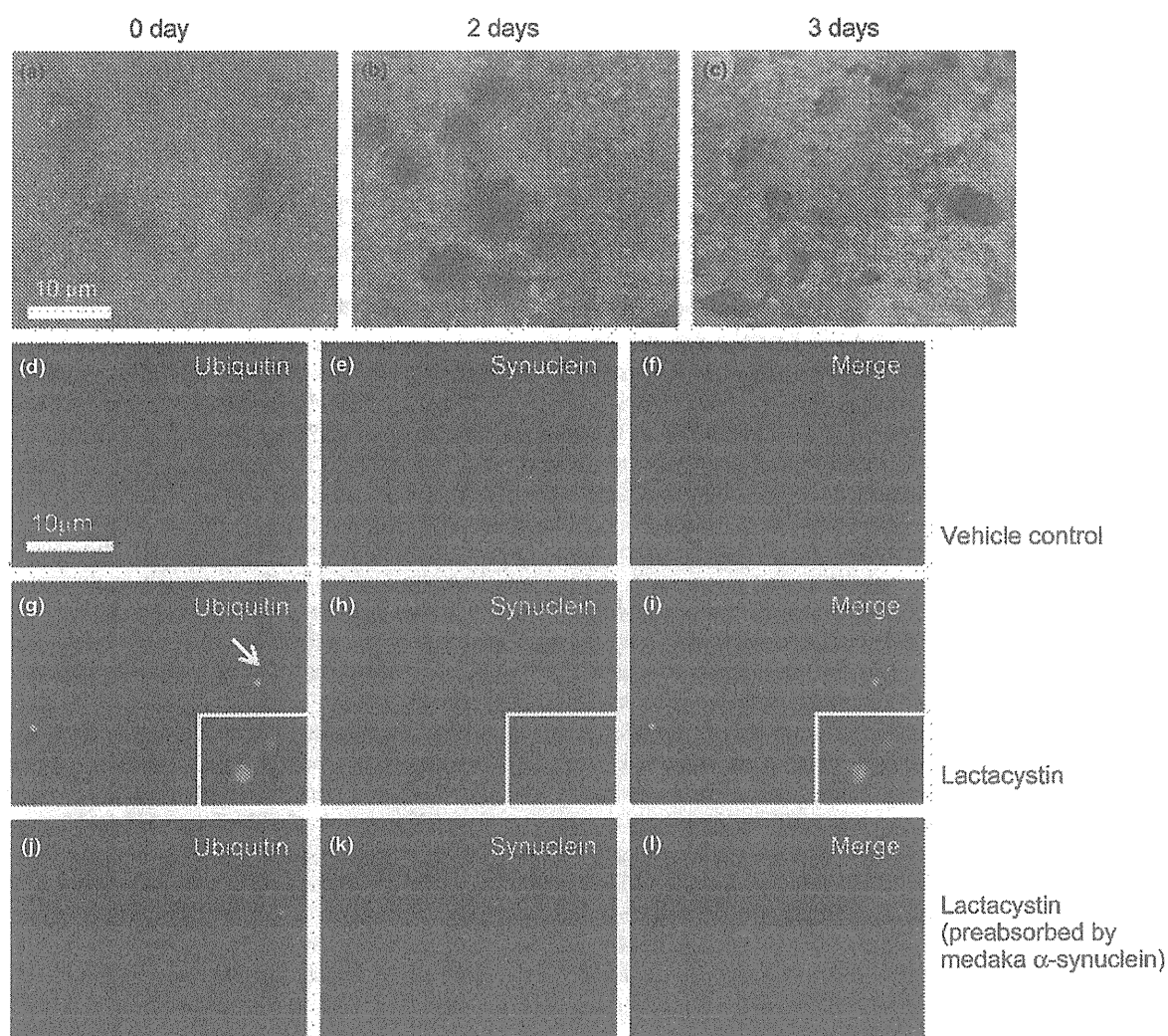

Fig. 4 Time course of ubiquitin-positive inclusion formation in lactacystin-treated medaka brain (anti-ubiquitin antibody, (DAB) staining) (a–c), and anti-synuclein antibody staining 3 days after the injection (d–l). (a) 0 day, soon after the injection. (b) 2 days after the injection. The nucleus and cytoplasm showed diffuse signal enhancement. (c) 3 days after the injection. Multiple ubiquitin-positive inclusions appeared. (d–f) Control brain. (g–l) Lactacystin-treated brain. (d, g, j) Anti-ubiquitin antibody staining. (e, h) Anti-synuclein antibody staining. (k) Pre-absorption by recombinant medaka α-synuclein (10 μg/mL) disappeared the signals of synuclein antibody, indicating this antibody indeed recognized medaka α-synuclein. (f) Merged image of (d) and (e). (i) Merged image of (g) and (h). (l) Ubiquitin and synuclein did not colocalize. Merged image of (j) and (k). Each inset of (g), (h) and (i) is an enlarged image of inclusions (arrows).

(Fig. 3c). Treatment with vehicle or 6-OHDA did not result in the formation of inclusion bodies (Fig. 3b and d).

To examine the detailed structure and localization of inclusions, samples were examined using transmission electron microscopy. Oval aggregates with multiple concentric and filamentous structures were observed in the cytoplasm (Fig. 3e–h). In some cases, lysosomes appeared to engulf these structures (Fig. 3e and f).

To check the time course of inclusion formation, we examined brain sections at 6 h, 1 day, 2 days and 3 days after the injection. General increase of ubiquitin was observed 1 and 2 days after the injection (Fig. 4b). Ubiquitin-positive inclusion bodies were first detected 3 days after the injection of lactacystin (Fig. 4c). Samples examined prior to 3 days post-injection did not appear to contain inclusion bodies (Fig. 4a and b).

Whether such ubiquitin-positive inclusion bodies correspond to Lewy bodies that are mainly composed of α-synuclein is an important question, we immunostained sections with an anti-synuclein antibody (Spillantini et al. 1997). The antigen of this antibody is the amino acids 11–26 of human α-synuclein (AKEGVVAAAEKTKQGV) and these amino acids sequences are well conserved between human and medaka (AKDGVVAAAKTKGV). Pre-absorption by recombinant medaka α-synuclein abolished the signals of synuclein antibody, indicating this antibody indeed recognized medaka α-synuclein. However, at all post-injection time points examined, infrequent colocalization of synuclein was observed with ubiquitin-positive inclusion bodies (Fig. 4d–l).

Fig. 5 Immunoblotting of TH, β-actin and tryptophan hydroxylase (TPH) in vehicle-, lactacystin- and 6-OHDA-treated medaka brain. (a) TH-specific reduction in lactacystin- and 6-OHDA-treated medaka brain. (b) Densitometric analysis of TH/β-actin band ($n = 8$). $^{**}p < 0.01$; $^{***}p < 0.001$.

Selective loss of dopaminergic and noradrenergic neurons in lactacystin-treated medaka

Immunoblotting of tryptophan hydroxylase and β-actin in lactacystin- and 6-OHDA-treated medaka brain were comparable to levels in the vehicle-treated group. However, TH signals in lactacystin- and 6-OHDA-treated medaka brain showed significant reductions, indicating specific cell loss of TH-positive neurons in these groups (Fig. 5a and b). To see whether lactacystin and 6-OHDA caused loss of dopaminergic neurons and fibers, immunohistochemistry was performed using anti-TH antibody. In medaka fish, dopaminergic neurons in the diencephalon are thought to contain an equivalent of dopaminergic neurons in human substantia nigra (Matsui et al. 2009). Vehicle-treated medaka showed intact TH-positive fibers in the striatum and normal TH-positive cell numbers in the diencephalon and medulla oblongata. In contrast, the TH-positive signals in the striatum decreased in lactacystin- and 6-OHDA-treated medaka (Fig. 6a–c and j). Furthermore, there was a significant decline in the number of TH-positive neurons in the middle diencephalon and locus coeruleus of lactacystin- and 6-OHDA-treated medaka brain (Fig. 6d–i, k and l). The numbers of Nissl-stained neurons in the optic tectum did not differ among vehicle-, lactacystin- and 6-OHDA-treated
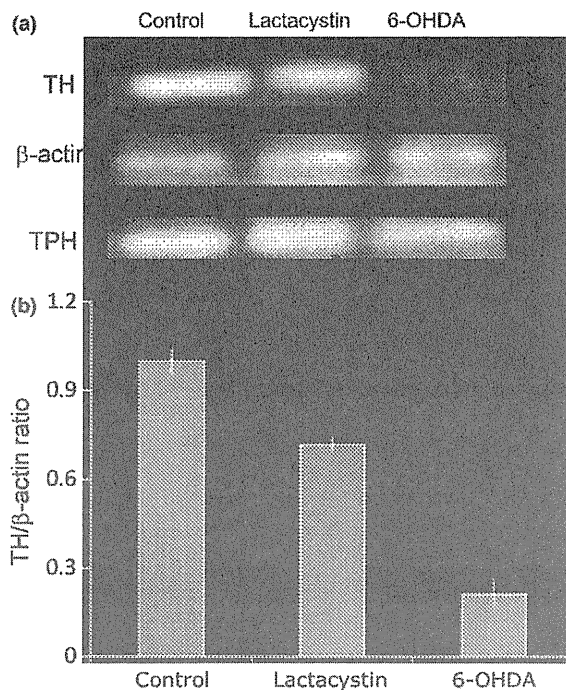
medaka (data not shown), indicating that the toxicity of lactacystin and 6-OHDA is specific to dopaminergic and noradrenergic neurons. The middle diencephalon and locus coeruleus were more affected than the caudal diencephalon, and the rostral diencephalon was totally spared (data not shown).

Next, we conducted TUNEL assay using the method previously described (Matsui et al. 2010). In the middle diencephalon of lactacystin-treated medaka brain, not in that of vehicle-treated one, TUNEL and TH double positive cells were observed (Fig. 6m–t). These findings indicated that lactacystin treatment indeed induced cell death of the TH-positive neurons in the middle diencephalon, with a fragmentation of DNA.

We used another proteasome inhibitor, epoxomicin. Epoxomicin treatment also led to inclusion body formation and similar immunohistochemical results (Fig. 7a–c). The specific vulnerability of TH-positive neurons in the middle diencephalon was also observed in epoxomicin-treated medaka (data not shown).

Finally, we measured the amount of catecholamine to confirm the effect of lactacystin and 6-OHDA on catecholamine neurons. Consistent with results from western blotting and immunohistochemistry, the amount of dopamine and
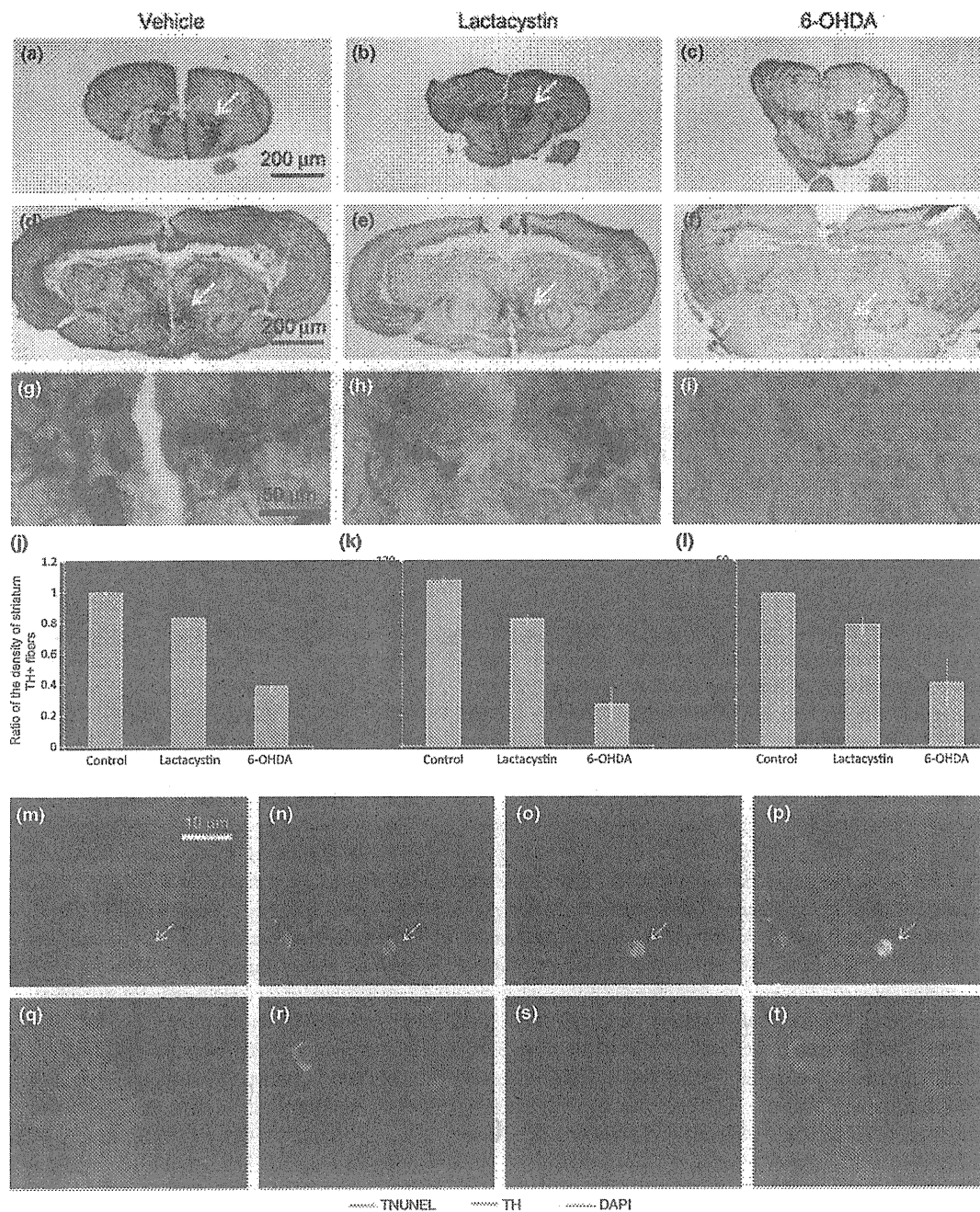
Fig. 6 TH immunohistochemistry of vehicle-, lactacystin- and 6-OHDA-treated medaka brain. (a–c) Forebrain. White arrows indicate TH-positive fibers in the striatum. (d–f) Middle diencephalon, low magnification. White arrows indicate TH-positive cell cluster. (g–i) Middle diencephalon, high magnification. (a, d, g) Vehicle-treated. (b, e, h) Lactacystin-treated. (c, f, i) 6-OHDA-treated. (j) Densitometric analysis of the striatum TH-positive fibers ($n = 4$). (k) TH-positive cell number of the middle diencephalon ($n = 8$). (l) TH-positive cell number of the locus coeruleus ($n = 8$). $^*p < 0.05$; $^{**}p < 0.01$; $^{***}p < 0.001$. (m–p) TUNEL and TH double-positive neurons in the middle diencephalon of lactacystin- (m–p) and vehicle- (q–t) treated medaka brain. (m, q) DAPI staining. (n, r) TH staining. (o, s) TUNEL staining. (p, t) Merged image of (m–o) and (q–s) respectively.

Fig. 7 Results of epoxomicin-treated medaka. (a) TH immunohistochemistry. The upper images show TH-positive fibers in the striatum (white arrow), and the middle (low magnification, white arrow indicates TH-positive cell cluster) and lower images (high magnification) show TH-positive neurons in the middle diencephalon. (b) Ubiquitin, TH-double positive neurons. White arrows indicate ubiquitin-positive inclusions. (c) The TH-positive cell number of the middle diencephalon ($n = 8$). ***$p < 0.001$.
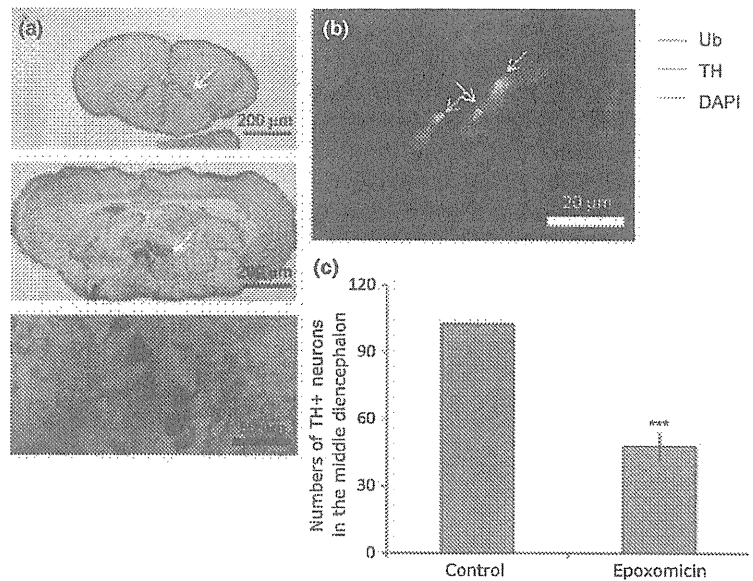
noradrenaline decreased significantly in lactacystin- and 6-OHDA-treated medaka brain. Differences in serotonin levels between treatment groups did not reach statistical significance (Fig. 8a–c). Together with the histological findings, we concluded that proteasome inhibition as well as 6-OHDA treatment caused selective loss of dopaminergic and noradrenergic neurons in medaka brain.

Decreased spontaneous movement in lactacystin-treated medaka

Because motor disturbances are one of the definite characteristics of PD, we evaluated the swimming movements of lactacystin- and 6-OHDA-treated medaka. Spontaneous movement of lactacystin- and 6-OHDA-treated medaka gradually reduced. Three days after the injections, swimming velocity was significantly reduced in lactacystin- and 6-OHDA-treated medaka compared with vehicle-treated fish. Total swimming distance also decreased in lactacystin- and 6-OHDA-treated medaka, but the reduction in 6-OHDA-treated fish did not reach statistical significance (Fig. 9a–d).

In conclusion, proteasome inhibition in medaka brain showed similarities not only to key pathologies of PD but also to motor disturbances seen in PD patients.

Discussion

Our results demonstrate that the administration of proteasome inhibitors to medaka via the CSF induces PD-like symptoms. Fish treated with lactacystin developed inclusion bodies similar to Lewy bodies, which are associated with PD. Although proteasome inhibition in medaka brain resulted in the formation of cytoplasmic inclusion bodies throughout the CNS, the absence of inclusion bodies in 6-OHDA-injected medaka brain suggests that formation of inclusion bodies is not secondary consequence of cell death. Treatment with lactacystin also induced selective loss of dopaminergic and noradrenergic neurons and a reduction in spontaneous movement. Using identical experimental parameters, we demonstrated that specific clusters of TH-positive neurons were especially vulnerable to toxins. All of the findings seen
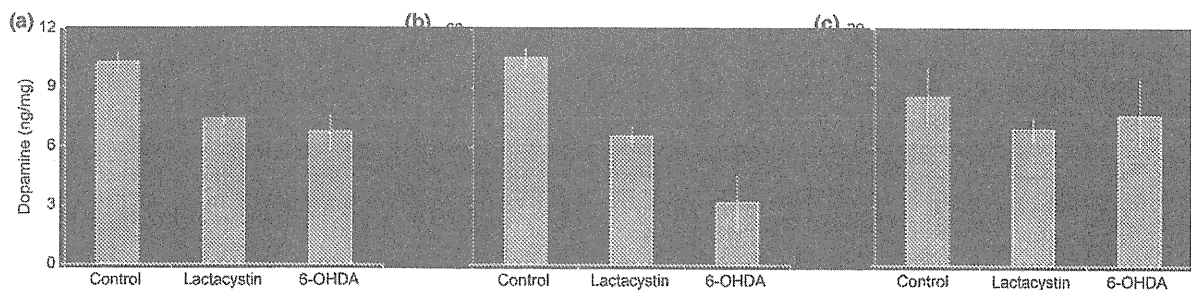

Fig. 8 HPLC analysis of catecholamine in vehicle-, lactacystin- and 6-OHDA-treated medaka brain ($n = 8$). (a) Dopamine. (b) Noradrenaline. (c) Serotonin ($n = 8$). *$p < 0.05$; **$p < 0.01$; ***$p < 0.001$.
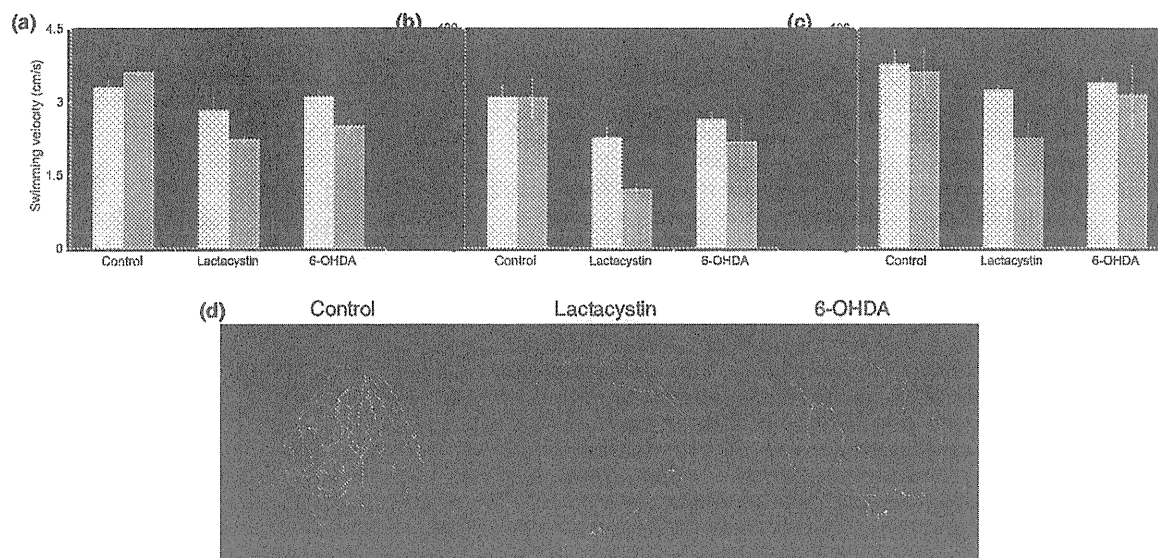
Fig. 9 Spontaneous swimming movement of vehicle-, lactacystin- and 6-OHDA-treated medaka (n = 8). Spontaneous swimming movement was assayed 1 (black) and 3 days (gray) after the injection. (a) Swimming velocity (cm/s). (b) Total swimming distance (cm). (c) Duration of swimming (s). (d) Representative tracks of medaka (n = 8). $*p < 0.05$; $**p < 0.01$; $***p < 0.001$.

in lactacystin-treated medaka brain were also replicated by another kind of proteasome inhibitors, epoxomicin (Fig. 7a–c). This strongly suggests that the formation of inclusion bodies was indeed a result of proteasome inhibition in medaka brain.

Lactacystin, epoxomicin, 6-OHDA and MPTP (Matsui et al. 2009) cause selective loss of dopaminergic and noradrenergic neurons in medaka. TH-positive neurons in the middle diencephalon and locus coeruleus showed marked vulnerability to different kinds of toxins compared with other neuron clusters. The reason for this selective vulnerability is unknown, but in medaka the TH-positive neurons in the middle diencephalon and locus coeruleus have relatively large cell bodies with well-developed fibers. In rats, the nigro-striatal dopaminergic neurons also have widespread fibers (Matsuda et al. 2009). Large neurons may require more optimal conditions for survival and this may explain the increased vulnerability of these cells.

Because lactacystin-treated medaka demonstrated more severe deficit in the behavioral tests compared with 6-OHDA-treated medaka, there may be non-catecholaminergic effects that were not detected in our assays. Lactacystin may affect other neuronal or non-neuronal behavioral system. Further studies would be needed.

The present results are consistent with prior findings in rats demonstrating PD-like symptoms in proteasome inhibitors-treated animals (McNaught et al. 2004). Although the results from the earlier report have not been consistently replicated, our findings demonstrate that proteasome inhibitors are

effective dopaminargic neurotoxins and may offer a good model for PD. Furthermore, the medaka is an appropriate model for testing neurochemical treatments because of the high level of accessibility to the CSF and brain. The easy accessibility of the CSF in medaka may help reduce differences in bioavailability of injected chemicals, one of the limitations of rat models.

One thing that our medaka model differed from human PD is the absence of colocalization of ubiquitin and synuclein in the inclusions. It may be due to the sensitivity of antibody we used or acute proteasome inhibition could not produce ubiquitin/synuclein double-positive inclusions. Our current aim is to replicate not only the selective loss of dopaminergic/noradrenergic neurons and movement disorders but also the formation of Lewy bodies.

Apart from the report by McNaught et al. and subsequent studies of proteasome inhibition in rats, this is the first study to show the loss of specific dopaminergic and noradrenergic neurons induced by the inhibition of proteasome activity. Recently, Meyer and his colleagues used the Cre-recombinase/loxP genetic approach to ablate the proteasomal Psmc1 ATPase gene and deplete 26S proteasomes in neurons in different regions of the brain to mimic neurodegeneration. Depletion of the gene in dopaminergic neurons in the substantia nigra generates a model of dopaminergic neurodedgeneration accompanied by Lewy pathology, further supporting the idea that proteasome inhibition leads to Parkinson's disease phenotype (Bedford et al. 2008). We believe that medaka can serve as a very useful model organism for PD research.

Acknowledgements

Supporting information

Additional supporting Information may be found in the online version of this article:

Movie S1. The movie of injection procedure. Detailed information is mentioned at the Materials and methods section.

As a service to our authors and readers, this journal provides supporting information supplied by the authors. Such materials are peer-reviewed and may be re-organized for online delivery, but are not copy-edited or typeset. Technical support issues arising from supporting information (other than missing files) should be addressed to the authors.

References

Beal F. and Lang A. (2006) The proteasomal inhibiton model of Parkinson's disease: "boon or bust"? *Ann. Neurol.* 60, 158–161.

Bedford L., Hay D., Devoy A. *et al.* (2008) Depletion of 26S proteasomes in mouse brain neurons causes neurodegeneration and Lewy-like inclusions resembling human pale bodies. *J. Neurosci.* 28, 8189–8198.

Bové J., Zhou C., Jackson-Lewis V., Taylor J., Chu Y., Rideout H. J., Wu D. C., Kordower J. H., Petrucelli L. and Przedborski S. (2006) Proteasome inhibition and Parkinson's disease modeling. *Ann. Neurol.* 60, 260–264.

Cook C. and Petrucelli L. (2009) A critical evaluation of the ubiquitin-proteasome system in Parkinson's disease. *Biochim. Biophys. Acta* 1792, 664–675.

Dawson T. M. and Dawson V. L. (2003) Molecular pathways of neurodegeneration in Parkinson's disease. *Science* 302, 819–822.

Kitada T., Asakawa S., Hattori N., Matsumine H., Yamamura Y., Minoshima S., Yokochi M., Mizuno Y. and Shimizu N. (1998) Mutations in the parkin gene cause autosomal recessive juvenile Parkinsonism. *Nature* 392, 605–608.

Kordower J. H., Kannan N. M., Chu Y., Suresh Babu R., Stansell J., III, Terpstra B. T., Sortwell C. E., Steece-Collier K. and Collier T. J. (2006) Failure of proteasome inhibitor administration to provide a model of Parkinson's disease in rats and monkeys. *Ann. Neurol.* 60, 264–268.

Leroy E., Boyer R., Auburger G. *et al.* (1998) The ubiquitin pathway in Parkinson's disease. *Nature* 395, 451–452.

Manning-Boğ A. B., Reaney S. H., Chou V. P., Johnston L. C., McCormack A. L., Johnston J., Langston J. W. and Di Monte D. A. (2006) Lack of nigrostriatal pathology in a rat model of proteasome inhibition. *Ann. Neurol.* 60, 256–260.

Matsuda W., Furuta T., Nakamura K. C., Hioki H., Fujiyama F., Arai R. and Kaneko T. (2009) Single nigrostriatal dopaminergic neurons form widely spread and highly dense axonal arborizations in the neostriatum. *J. Neurosci.* 29, 444–453.

Matsui H., Taniguchi Y., Inoue H., Uemura K., Takeda S. and Takahashi R. (2009) A chemical neurotoxin, MPTP induces Parkinson's disease like phenotype, movement disorders and persistent loss of dopamine neurons in medaka fish. *Neurosci. Res.* 65, 263–271.

Matsui H., Taniguchi Y., Inoue H., Kobayashi Y., Sakaki Y., Toyoda A., Uemura K., Kobayashi D., Takeda S. and Takahashi R. (2010) Loss of PINK1 in medaka fish (Oryzias latipes) causes late-onset decrease in spontaneous movement. *Neurosci. Res.* 66, 151–161.

McNaught K. S. and Olanow C. W. (2006a) Proteasome inhibitor-induced model of Parkinson's disease. *Ann. Neurol.* 60, 243–247.

McNaught K. S., Perl D. P., Brownell A. L. and Olanow C. W. (2004) Systemic exposure to proteasome inhibitors causes a progressive model of Parkinson's disease. *Ann. Neurol.* 56, 149–162.

McNaught K. S., Jackson T., JnoBaptiste R., Kapustin A. and Olanow C. W. (2006b) Proteasomal dysfunction in sporadic Parkinson's disease. *Neurology* 66, S37–S49.

Nair V. D., McNaught K. S., González-Maeso J., Sealfon S. C. and Olanow C. W. (2006) p53 mediates nontranscriptional cell death in dopaminergic cells in response to proteasome inhibition. *J. Biol. Chem.* 281, 39550–39560.

Schapira A. H., Cleeter M. W., Muddle J. R., Workman J. M., Cooper J. M. and King R. H. (2006) Proteasomal inhibition causes loss of nigral tyrosine hydroxylase neurons. *Ann. Neurol.* 60, 253–255.

Spillantini M. G., Schmidt M. L., Lee V. M., Trojanowski J. Q., Jakes R. and Goedert M. (1997) Alpha-synuclein in Lewy bodies. *Nature* 388, 839–840.

Tofaris G. K., Razzaq A., Ghetti B., Lilley K. S. and Spillantini M. G. (2003) Ubiquitination of alpha-synuclein in Lewy bodies is a pathological event not associated with impairment of proteasome function. *J. Biol. Chem.* 278, 44405–44411.

Zeng B. Y., Bukhatwa S., Hikima A., Rose S. and Jenner P. (2006) Reproducible nigral cell loss after systemic proteasomal inhibitor administration to rats. *Ann. Neurol.* 60, 248–252.

Neurobiology of Disease

Induced Loss of ADAR2 Engenders Slow Death of Motor Neurons from Q/R Site-Unedited GluR2

Takuto Hideyama,[1,2] Takenari Yamashita,[1,2] Takeshi Suzuki,[3] Shoji Tsuji,[2] Miyoko Higuchi,[5] Peter H. Seeburg,[5] Ryosuke Takahashi,[6] Hidemi Misawa,[4] and Shin Kwak[1,2]

[1]Core Research for Evolutional Science and Technology, Japan Science and Technology Agency and [2]Department of Neurology, Graduate School of Medicine, University of Tokyo, Bunkyo-ku, Tokyo 113-8655, Japan, [3]Division of Basic Biological Sciences and [4]Department of Pharmacology, Faculty of Pharmacy, Keio University, Minato-ku, Tokyo 105-8512, Japan, [5]Department of Molecular Neuroscience, Max Planck Institute of Medical Research, 69120 Heidelberg, Germany, and [6]Department of Neurology, Graduate School of Medicine, University of Kyoto, Sakyo-ku, Kyoto 606-8507, Japan

GluR2 is a subunit of the AMPA receptor, and the adenosine for the Q/R site of its pre-mRNA is converted to inosine (A-to-I conversion) by the enzyme called adenosine deaminase acting on RNA 2 (ADAR2). Failure of A-to-I conversion at this site affects multiple AMPA receptor properties, including the Ca^{2+} permeability of the receptor-coupled ion channel, thereby inducing fatal epilepsy in mice (Brusa et al., 1995; Feldmeyer et al., 1999). In addition, inefficient GluR2 Q/R site editing is a disease-specific molecular dysfunction found in the motor neurons of sporadic amyotrophic lateral sclerosis (ALS) patients (Kawahara et al., 2004). Here, we generated genetically modified mice (designated as AR2) in which the ADAR2 gene was conditionally targeted in motor neurons using the Cre/loxP system. These AR2 mice showed a decline in motor function commensurate with the slow death of ADAR2-deficient motor neurons in the spinal cord and cranial motor nerve nuclei. Notably, neurons in nuclei of oculomotor nerves, which often escape degeneration in ALS, were not decreased in number despite a significant decrease in GluR2 Q/R site editing. All cellular and phenotypic changes in AR2 mice were prevented when the mice carried endogenous GluR2 alleles engineered to express edited GluR2 without ADAR2 activity (Higuchi et al., 2000). Thus, loss of ADAR2 activity causes AMPA receptor-mediated death of motor neurons.

Introduction

GluR2 (also known as GluR-B or GluA2) is a subunit of the AMPA receptor. The adenosine within the glutamine codon for the Q/R site of its pre-mRNA is converted to inosine (A-to-I conversion) (Yang et al., 1995) by adenosine deaminase acting on RNA 2 (ADAR2) (Melcher et al., 1996). Because inosine is read as guanosine during translation, the genomic glutamine codon (Q: CAG) is converted to a codon for arginine (R: CIG) at the Q/R site of GluR2 in virtually all neurons in the mammalian brain (Seeburg, 2002). Conversion of Q to R at the Q/R site of GluR2 affects multiple AMPA receptor properties, including the Ca^{2+} permeability of the receptor-coupled ion channel, receptor trafficking, and assembly of receptor subunits (Sommer et al., 1991; Burnashev et al., 1992; Greger et al., 2002, 2003). Genetically modified mice in which the Q/R site of GluR2 remains unedited displayed fatal status epilepticus at early postnatal stages with exaggerated excitation of neurons (Brusa et al., 1995; Feldmeyer et al., 1999). Systemic ADAR2-null mice exhibit a similar phenotype, which

was attributed to the absence of GluR2 Q/R site RNA editing (Higuchi et al., 2000). These findings indicate that the A-to-I conversion of the GluR2 Q/R site by ADAR2 is crucial for survival in mice. However, it has not been demonstrated whether neuronal death occurs in mice lacking GluR2 Q/R site editing or in those lacking ADAR2.

Amyotrophic lateral sclerosis (ALS) is the most common adult-onset motor neuron disease. Patients with sporadic ALS account for >90% of all cases, and the majority of them do not carry mutations in the causative genes of familial ALS that have been identified thus far (Schymick et al., 2007; Beleza-Meireles and Al-Chalabi, 2009). There is strong evidence indicating that AMPA receptor-mediated excitotoxic mechanism plays a pathogenic role in ALS and SOD1-associated familial ALS model animals (Rothstein et al., 1992; Carriedo et al., 1996; Van Damme et al., 2005). Recently, we demonstrated that a significant proportion of GluR2 mRNA was unedited at the Q/R site in spinal motor neurons of postmortem patients with sporadic ALS. This is in marked contrast to the fact that all GluR2 mRNA was edited in the motor neurons of control subjects (Takuma et al., 1999; Kawahara et al., 2004) and of patients with motor neuron diseases other than sporadic ALS (Kawahara et al., 2006), as well as in dying neurons in other neurodegenerative diseases, including Purkinje cells of patients with spinocerebellar degeneration (Paschen et al., 1994; Akbarian et al., 1995; Kawahara et al., 2004; Suzuki et al., 2003). The disease specificity of inefficient GluR2 Q/R site editing implies the pathogenic relevance of ADAR2 insufficiency in the death of motor neurons in sporadic ALS but

leaves open the possibility that other genes whose products remain unedited by ADAR2 insufficiency might contribute to the demise of motor neurons.

We therefore generated a conditional ADAR2 knock-out mouse strain (designated here as AR2), using the Cre/loxP recombination system, and demonstrated that the loss of ADAR2 activity induces the slow death of motor neurons also in the mouse. Importantly, all motor neuron death in AR2 mice could be prevented by substituting the wild-type GluR2 alleles for alleles point mutated to express Q/R site-edited GluR2 in the absence of ADAR2. Our genetic studies in the mouse clearly demonstrate that the underediting of the GluR2 Q/R site specifically induces death of motor neurons with reduced ADAR2 activity.

Materials and Methods

All studies were performed in accordance with the Declaration of Helsinki, the Guideline of Animal Studies of the University of Tokyo, and National Institutes of Health. The committee of animal handling of the University of Tokyo also approved the experimental procedures used.

ADAR2 flox allele and conditional ADAR2 knock-out mice. DNA for the targeted region was obtained from a mouse strain 129/SvEv genomic library (supplemental Table S1, available at www.jneurosci.org as supplemental material). A LoxP site was inserted into intron 6 and another LoxP site was inserted into intron 9 of the mouse *ADAR2* gene (*adarb1*), along with a selection cassette containing a neomycin resistance gene (Neo) flanked by flippase recognition target (FRT) sites (Fig. 1A). Exons 7–9 encode the majority of the adenosine deaminase motif. Chimeric mice were generated by injection of a targeted embryonic stem cell clone into C57BL/6-derived blastocysts. *ADAR2$^{flox/+}$* intercrosses produced *ADAR2$^{flox/flox}$* mice at apparent Mendelian frequencies, and *ADAR2$^{flox/flox}$* homozygous mice were phenotypically normal. Determination of the *ADAR2^{flox}* allele was conducted by genomic PCR (Fig. 1B). Then, to knock-out ADAR2 activity selectively in motor neurons, we crossed *ADAR2$^{flox/flox}$* mice with VAChT–Cre.Fast mice to obtain AR2 mice.

AR2 mice. Intercrosses of *ADAR2$^{flox/+}$*/VAChT–Cre.Fast mice produced *ADAR2$^{flox/flox}$*/VAChT–Cre.Fast (AR2) mice, either heterozygous or homozygous for the Cre transgene, which directs restricted Cre expression under the control of the vesicular acetylcholine transporter gene promoter in a subset of cholinergic neurons, including the spinal motor neurons (Misawa et al., 2003). Cre expression levels were found not to differ in mice heterozygous or homozygous for the VAChT–Cre.Fast transgene (Misawa et al., 2003). The same intercrosses also produced, as littermates of AR2, *ADAR2$^{flox/flox}$* (Ctl1) and *ADAR2$^{+/+}$*/VAChT–Cre-.Fast mice (Ctl2), which were used as controls. Both genders of AR2 and control mice were used, but littermates heterozygous for the floxed ADAR2 allele were not used in this study. All genotyping was performed by PCR on DNA from tail biopsies. PCR primers and amplicon sizes for the different alleles are listed in supplemental Table S1 (available at www. jneurosci.org as supplemental material).

AR2/GluR-B$^{R/R}$ mice. AR2/GluR-B$^{R/R}$ mice were generated by intercrossing ADAR2$^{flox/+}$/VAChT–Cre.Fast/GluR-B$^{R/+}$ mice, which had been produced by crossbreeding AR2 mice with GluR-B$^{R/R}$ mice. The AR2/GluR-B$^{R/R}$ mice used by us were either heterozygous or homozygous for the Cre transgene (Misawa et al., 2003) and homozygous for the floxed ADAR2 and the GluR-B(R) allele. The desired genotype was found approximately once in every 20 offspring. Other genotypes produced by the intercrosses were not used in this study. All genotyping for the ADAR2 and GluR2 (GluR-B) alleles as well as for the Cre transgene was by PCR on DNA extracted from tail biopsies. PCR primers and amplicon sizes for the different alleles are listed in supplemental Table S1 (available at www.jneurosci.org as supplemental material).

Genomic PCR and reverse transcription-PCR. Genomic DNA was extracted from mouse tails using the High Pure PCR Template Preparation kit (Roche). Total RNA was isolated from brain and spinal cord tissue, and first-strand cDNA was synthesized and then treated with DNase I (Invitrogen) as described previously (Kawahara et al., 2003b). Primer

pairs and the conditions used for PCR are presented in supplemental Table S1 (available at www.jneurosci.org as supplemental material). Positions of primer pairs used for genomic ADAR2 PCR (Fig. 1A, F1/R1) and ADAR2 reverse transcription (RT)-PCR (Fig. 1C, F2/R2) are indicated.

Analysis for editing efficiency at A-to-I sites. Editing efficiencies at the Q/R sites in GluR2 mRNAs were calculated by quantitative analyses of the digests of RT-PCR products with BbvI as described previously (Takuma et al., 1999; Kawahara et al., 2003a, 2004). In brief, 2 μl of cDNA were subjected to first PCR in duplicate in a reaction mixture of 50 μl containing 200 mM each primer, 1 mM dNTP Mix (Eppendorf), 5 μl of 10× PCR buffer, and 1 μl of Advantage 2 Polymerase mix (Clontech). The PCR amplification began with a 1 min denaturation step at 95°C, followed by 40 cycles of denaturation at 95°C for 10 s, annealing at 60°C for 30 s, and extension at 68°C for 40 s. Nested PCR was conducted on 2 μl of the first PCR product under the same conditions with the exception of the annealing temperature (58°C). Primer pairs used for each PCR were listed in supplemental Table S1 (available at www.jneurosci.org as supplemental material). After gel purification using the Zymoclean Gel DNA Recovery kit according to the protocol of the manufacturer (Zymo Research), an aliquot (0.5 mg) was incubated with BbvI (New England Biolabs) at 37°C for 12 h. The PCR products originating from Q/R site-edited GluR2 mRNA had one intrinsic restriction enzyme recognition site, whereas those originating from unedited mRNA had an additional recognition site. Thus, restriction digestion of the PCR products originating from edited GluR2 mRNA should produce different numbers of fragments (two bands at 219 and 59 bp) from those originating from unedited GluR2 mRNA (three bands at 140, 79, and 59 bp). Because the 59 bp band would originate from both edited and unedited mRNA but the 219 bp band would originate from only edited mRNA, we quantified the molarity of the 219 and 59 bp bands using the 2100 Bioanalyzer (Agilent Technologies) and calculated the editing efficiency as the ratio of the former to the latter for each sample (supplemental Table S1, available at www.jneurosci.org as supplemental material)

With similar methods, we calculated the editing efficiencies at the Q/R sites in GluR5 and GluR6 mRNA and in GluR2 pre-mRNA, the R/G site in GluR2 mRNA, and the I/V site in Kv1.1 mRNA (Paschen et al., 1994; Takuma et al., 1999; Kawahara et al., 2003a, 2004; Nishimoto et al., 2008). The following restriction enzymes were used for restriction digestion of the respective A-to-I sites: BbvI for the Q/R sites, MfeI (New England Biolabs) for the I/V site, and MseI (New England Biolabs) for the R/G site. Primer pairs used for each PCR and sizes of restriction digests of PCR products were indicated in supplemental Table S1 (available at www.jneurosci.org as supplemental material).

Behavioral analyses. Using a mouse-specific rotarod (SN-445; Neuroscience Corp.), we determined the maximal time before falling at 10 rpm during a 180 s period; each run consisted of three trials. Grip strength was measured with a dynamometer (NS-TRM-M; Neuroscience Corp.). Measurements were conducted weekly by a researcher blind to genotype and age of the mice.

Isolation of single motor neurons and brain tissue. Single-cell isolation from frozen spinal cord tissue was performed with a laser microdissection system (Leica AS LMD; Leica Microsystems) as described previously (Kawahara et al., 2003b, 2004). All of the large motor neurons (diameter larger than 20 μm) in the anterior horn were dissected from 14-μm-thick cervical cord sections, and three neurons each were collected together into respective single test tubes containing 200 μl of TRIZOL Reagent. In addition, using the same method, nuclei of oculomotor nerve and of facial nerve were dissected from the brainstem sections of AR2 mice and control mice at 12 months of age. The positions of these cranial nerve nuclei were identified using the Paxinos and Franklin mouse brain atlas (Paxinos and Franklin, 2001). All samples were kept at −20°C until use.

Immunohistochemistry. Under deep anesthesia with isoflurane, mice were transcardially perfused with 3% paraformaldehyde and 1% glutaraldehyde in PBS. The brains and spinal cords were removed and immersed in serially increasing concentrations of a sucrose–PBS solution (final sucrose concentration of 30%). The immunohistochemical procedure was performed on 10-μm-thick sections, which were cut with a cryostat (model HM500 O; Microm). The sections were analyzed with a
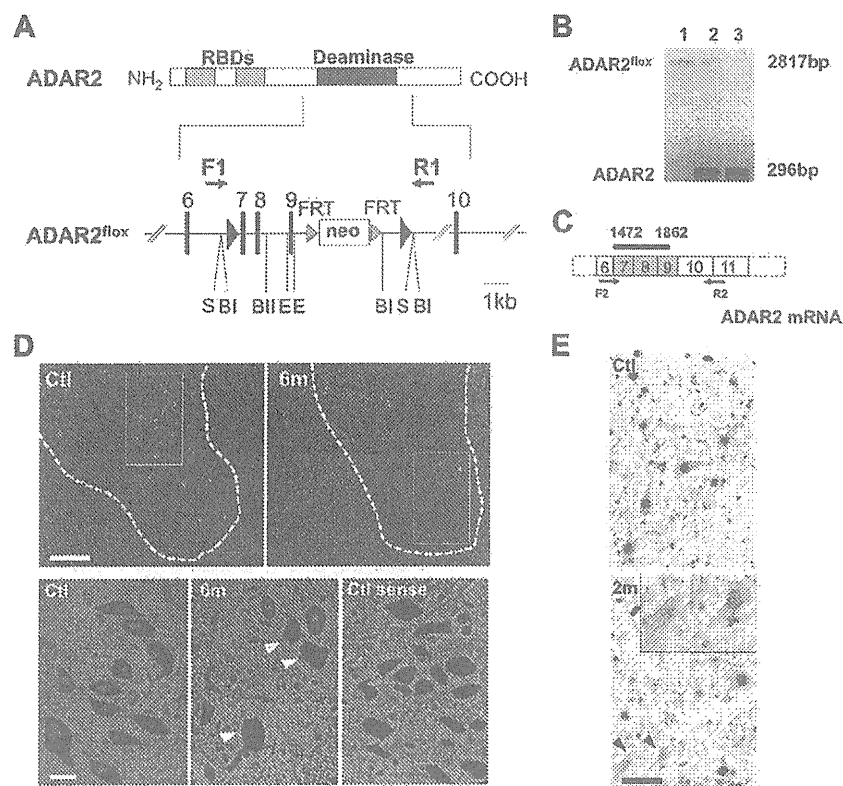
Figure 1. Generation of a conditional ADAR2 knock-out mouse. *A*, A LoxP site (filled triangle) was inserted into intron 6 and another LoxP site in intron 9 with a selection cassette containing the gene for neomycin resistance (Neo) flanked by FRT sites. Exons are depicted as black bars with numbers. RBDs, RNA binding domains; F1/R1, primer pair (supplemental Table S1, available at www.jneurosci.org as supplemental material) for *B*; S, Sfil; Bl, Bgll; Bll, Bglll; E, ERI. *B*, Genomic PCR using template DNA obtained from the tails of ADAR2*flox/flox* mice (lane 1), ADAR2*flox/+* mice (lane 2), and ADAR2*+/+* mice (lane 3). *C*, Exons excised by recombination are shown as shaded areas in the mRNA, and a black bar indicates the *in situ* hybridization probe (supplemental Table S1, available at www.jneurosci.org as supplemental material) for *D*. F2/R2, Primer pair (supplemental Table S1, available at www.jneurosci.org as supplemental material) used in Figure 2 *B*. *D*, *In situ* hybridization using a probe that encompasses the region excised by Cre-mediated recombination. There is a large number of punctate signals in the gray matter (outlined with dotted lines) of control mice (Ctl), whereas nuclei of some large neurons in the anterior horn were devoid of signal in the ADAR2*flox/flox*/VAChT–Cre.Fast (AR2) mice at 6 months of age (6m; arrowheads in magnified view). The sense probe did not yield a visible signal in the control mice at the same age (Ctl sense). Scale bars: top panels, 200 μm; bottom panels, 25 μm. *E*, All SMI-32-positive large neurons in the anterior horn (AHCs, brown color in the cytoplasm) of the cervical cord (C5) were ADAR2 positive (dark gray color in the nuclei) in the control mice (Ctl), whereas some of them were devoid of ADAR2 immunoreactivity in AR2 mice at 2 months of age (2m, arrowheads and inset). Sections were counterstained with hematoxylin. Scale bar: 50 μm; inset, 25 μm.

synaptophysin (dilution at 1:100; Cell Signaling Technologies) and then with Alexa Fluor 488 rabbit anti-mouse IgG (dilution at 1:100; Invitrogen) as the secondary antibody. Stained sections were examined under an LSM-510 confocal microscope system (Carl Zeiss).

Electrophysiology. Mice were anesthetized with isoflurane and placed in a prone position on a thermal pad at 37°C for the examination. Electromyogram (EMG) recordings using a Power Lab 26T and EMG machine (AD Instruments) were obtained using a 29-gauge, Teflon-coated, monopolar needle electrode. The recording electrode was inserted into the gastrocnemius muscles, and spontaneous electrical activity was recorded for 120 s using a Lab Chart analysis system (AD Instruments).

Morphological observation and stereology. Sections of the fifth cervical (C5) and fifth lumbar (L5) spinal cord segments were sequentially immunostained with RED1 and SMI-32 using the HRP–DAB system with and without the addition of $NiCl_2$ for color development. Some sections were immunostained with NeuN. ADAR2-positive and -negative neurons were separately counted among SMI-32-positive neurons with diameters larger than 20 μm in 10 sections for each mouse. The number of NeuN-positive neurons with diameter smaller than 20 μm in the ventral gray matter (ventral to the line running though the ventral edge of the central canal) was counted in 10 C5 sections for each mouse at 12 months of age. None of the NeuN-positive small neurons exhibited SMI-32 or GFAP immunoreactivity. The entire brainstem of each mouse at 12 months of age was cut axially to produce a 10-μm-thick section, and the numbers of all the neurons with nucleoli in the nuclei of cranial motor nerves were counted under a light microscope after cresyl violet staining. The position of each nucleus was stereologically determined using a mouse brain atlas (Paxinos and Franklin, 2001). The positions from the bregma were from −3.80 to −4.24 mm (nucleus of oculomotor nerve), from −4.36 to −4.48 mm (nucleus of trochlear nerve), from −4.84 to −5.34 mm (motor nucleus of trigeminal nerve), from −5.52 to −5.80 mm (nucleus of abducens nerve), from −5.68 to −6.48 mm (nucleus of facial nerve), from −7.08 to −7.92 mm (dorsal nucleus of vagus nerve), and from −7.08 to −8.12 mm (nucleus of hypoglossal nerve). The density of neurons in each nucleus was estimated by dividing the total number of neurons in each nucleus by the volume of the nucleus, which was calculated as the product of the area of the nucleus and the thickness of each section. In addition, transverse, 1-μm-thick, Epon-embedded sections of the anterior horns of the spinal cord, and the ventral roots at the L5 level were prepared and stained with 0.1% toluidine blue. Cell counting was performed by researchers who were blind to the genotype of the mouse.

In situ hybridization. Anesthetized mice were perfusion fixed with Tissue Fixative (GenoStaff). Dissected cervical cord tissues were sectioned after they were embedded in paraffin. Antisense and sense *adarb1* cRNA probes (Fig. 1C) (supplemental Table S1, available at www.jneurosci.org as supplemental material) were generated from the mouse *adarb1* open reading frame sequence, which was cloned into the pGEMT-Easy vector (Promega). Digoxigenin-labeled cRNA probes were prepared with the DIG RNA Labeling mix (Roche Applied Science). Color was developed with nitro blue tetrazolium/5-bromo-4-chloro-3-indolyl phosphate, and tissue sections were counterstained with Kernechtrot stain solution

standard avidin–biotin–immunoperoxidase complex method using the M.O.M. Immunodetection kit (Vector Laboratories) for mouse primary antibodies and Vectastain ABC IgGs (Vector Laboratories) for other primary antibodies. The following primary antibodies were used: mouse anti-nonphosphorylated neurofilament H (SMI-32; dilution at 1:1000; Covance), mouse anti-neuronal nuclei (NeuN) (dilution at 1:500; Millipore Bioscience Research Reagents), sheep anti-rat RED1 (ADAR2) N terminus [dilution at 1:500; a gift from Dr. R. B. Emeson (Sansam et al., 2003)], rabbit anti-glial fibrillary acidic protein (GFAP) (dilution at 1:200; Lab Vision), and rat anti-mouse MAC-2 (dilution at 1:500; Cedarlane). Color was developed with the HRP–DAB System (Vector Laboratories).

Muscles and neuromuscular junctions. Medial gastrocnemius muscles and medial quadriceps muscles were dissected, pinned in mild stretch, and mounted on cork blocks and were quickly frozen in isopentane–liquid nitrogen. Samples were stored at −80°C until use. Five-micrometer-thick transverse frozen sections were stained with hematoxylin and eosin. Twenty-micrometer-thick frozen longitudinal sections were stained with tetramethylrhodamine–bungarotoxin. The same section was incubated with monoclonal antibodies to neurofilament (NF160; dilution at 1:200; Millipore Bioscience Research Reagents) and

(Muto Pure Chemicals). After mounting, 24-bit color images were acquired by scanning of the sections. Digoxigenin signals were isolated by uniformly subtracting the counterstaining color component using Photoshop version 9.0.2 (Adobe Systems) (Ohmae et al., 2006; Takemoto-Kimura et al., 2007).

Statistics. Differences in behavior and survival rates between groups were analyzed using log-rank analysis with SPSS software (version 15; SPSS Inc.), and GraphPad Prism version 4 (GraphPad Software), respectively. The differences in neuronal number between each group and the control samples were examined with a repeated-measures ANOVA. The SPSS version 15 software was used for ANOVA, followed by a Tukey–Kramer statistical test.

Results

Generation of the $ADAR2^{flox/flox}$/VAChT–Cre mouse, designated as AR2 mouse

We constructed the mouse $ADAR2^{flox}$ allele by flanking exons 7–9 of the *adarb1* gene (mouse *ADAR2* gene) with loxP sites (Fig. 1A) (supplemental Table S1, available at www.jneurosci.org as supplemental material). Exons 7–9 encode the majority of the adenosine deaminase motif in the *adarb1* gene (Feng et al., 2006), and Cre-mediated deletion of this region ablates ADAR2 activity. To ablate ADAR2 activity selectively in motor neurons, we crossed $ADAR2^{flox/flox}$ mice with VAChT–Cre.Fast mice. In VAChT–Cre.Fast mice, Cre expression is under the control of the vesicular acetylcholine transporter gene promoter, which is active in cholinergic neurons, including spinal motor neurons (Misawa et al., 2003). In these transgenic mice, Cre expression is developmentally regulated, and ~50% of motor neurons express Cre by 5 weeks of age, independent of the heterozygous or homozygous state of the transgene (Misawa et al., 2003). The resulting $ADAR2^{flox/flox}$/VAChT–Cre.Fast mice, referred to here as AR2 mice (for breeding, see Materials and Methods), therefore would lack ADAR2 activity in a subset of motor neurons in the spinal cord and other brain motor nuclei after expression of Cre by 5 weeks of age. *In situ* hybridization with a probe encompassing the sequence excised by Cre-mediated recombination (Fig. 1C) demonstrated that several large neurons in the anterior horn (AHCs) were devoid of *adarb1* gene signal in the AR2 mice, whereas all the AHCs exhibited the signal in control littermates (Fig. 1D). Similarly, a subset of the AHCs were devoid of ADAR2 immunoreactivity in AR2 mice, whereas all AHCs exhibited ADAR2 immunoreactivity in the controls (Fig. 1E). There was no difference in the results on male and female AR2 mice.

ADAR2 activity in ADAR2-null motor neurons

Next we examined the effects of recombination of the $ADAR2^{flox}$ allele on ADAR2 activity. We dissected all large neurons in the anterior horn (AHCs) (for AHC identification, see supplemental Fig. S1A, available at www.jneurosci.org as supplemental material) from frozen sections from 2-month-old AR2 mice ($n = 4$) using a laser microdissector (Fig. 2A). We verified that these AHCs, but not small neurons in the anterior horn, are the spinal motor neurons by RT-PCR for choline acetyltransferase on a single-cell lysates (supplemental Fig. S1, available at www.jneurosci.org as supplemental material). Because RT-PCR of GluR2 mRNA on the lysates of three neurons, but not the lysates of one or two motor neurons, reproducibly yielded amplification products, we analyzed the extent of GluR2 Q/R site editing on RNA extracted from the lysates of three pooled AHCs (designated as a specimen) by quantitative analysis of the BbvI-restriction digests of the RT-PCR products, as described previously (Kawahara et al., 2003b, 2004). Among 116 specimens examined, eight showed 0% and 42 showed 100% Q/R site editing, with the re-
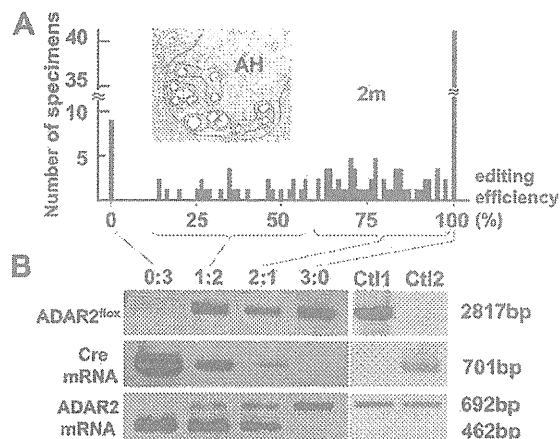

Figure 2. Cre-dependent targeting of ADAR2 and GluR2 Q/R site-editing in motor neurons. *A*, Frequency histogram of editing efficiency at the GluR2 Q/R site in specimens (lysates containing 3 motor neurons) obtained from AR2 mice at 2 months of age (2m; $n = 4$). Neurons were dissected with a laser microdissector (inset). *B*, Specimens ($n = 116$) were collected into four groups depending on the predicted number of ADAR2-deficient neurons in each specimen; the groups of specimens containing 3, 2, 1, and 0 unedited GluR2-expressing neurons were designated as groups 0:3, 1:2, 2:1, and 3:0, respectively. The $ADAR2^{flox}$ gene and transcripts of the *Cre* gene and the $ADAR2^{flox}$ alleles before and after recombination were analyzed for each group by PCR. AHCs expressing unedited GluR2 mRNA (group 0:3) harbored the truncated $ADAR2^{flox}$ gene and Cre transcripts, whereas AHCs expressing edited GluR2 mRNA (group 3:0) carried the full-length $ADAR2^{flox}$ gene and did not express Cre. Ctl1, $ADAR2^{flox/flox}$ mice; Ctl2, VAChT–Cre.Fast mice; AH, anterior horn of the spinal cord.

maining 66 specimens distributed between the ranges of 17 and 98% (Fig. 2A) (supplemental Table S2, available at www.jneurosci.org as supplemental material). Because AHCs of control littermates (these carried wild-type ADAR2 alleles or no Cre transgene; see Materials and Methods) expressed only edited GluR2 mRNA, the presence of samples exhibiting 0% Q/R site editing suggests that ADAR2-expressing neurons expressed only edited GluR2 mRNA, whereas ADAR2-null neurons expressed only unedited GluR2 mRNA. Then, DNA and total RNA from the specimens were collected in four different groups according to the proportions of unedited GluR2 (Fig. 2A). Using PCR, we demonstrated that the samples with 100% editing efficiency (group 0:3) harbored the truncated $ADAR2^{flox}$ gene and Cre transcripts, whereas the samples with 100% editing efficiency (group 3:0) carried the full-length $ADAR2^{flox}$ gene and did not express Cre (Fig. 2B). Those samples with both edited and unedited GluR2 mRNA (groups 1:2 and 2:1) exhibited both full-length and truncated ADAR2 along with the Cre transcript. These qualitative results are consistent with the assumption that recombination of the $ADAR2^{flox}$ alleles occurred in a Cre-dependent manner and that this recombination abolished the editing of the GluR2 Q/R site. Among other A-to-I sites examined, we found a significant reduction in editing efficiency only at the GluR6 Q/R site (supplemental Table S3, available at www.jneurosci.org as supplemental material).

Behavioral changes

AR2 mice were hypokinetic (supplemental movie, available at www.jneurosci.org as supplemental material) and abnormal in posture (supplemental Fig. S2A, available at www.jneurosci.org as supplemental material), but they displayed no overt paralysis or vesico-urinary disturbances and exhibited a normal withdrawal response to noxious stimuli. They showed a lower rotarod performance than their control littermates after 5 weeks of age
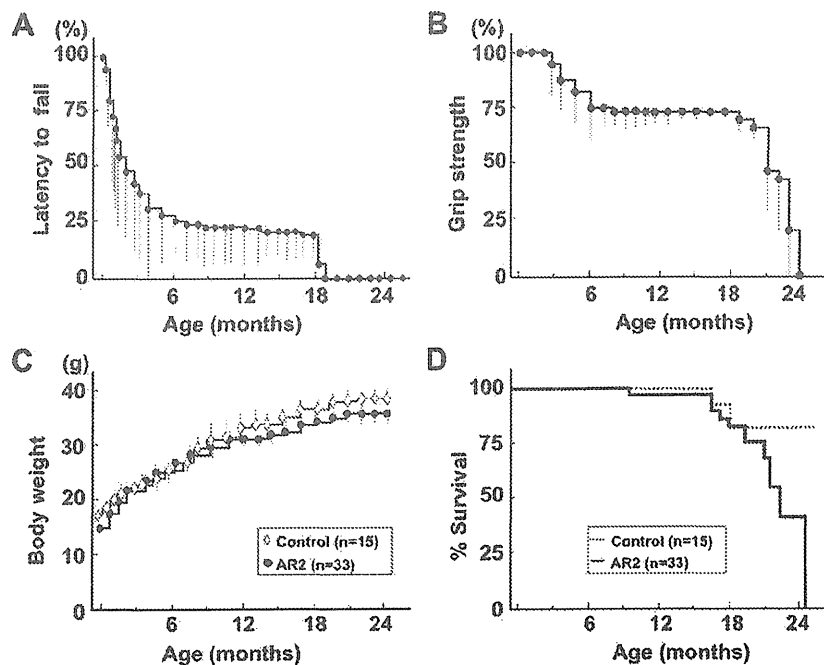
Figure 3. Behavioral changes in AR2 mice. *A*, Rotarod performance presented as latency to fall (at 10 rpm, 180 s at the maximum) began to decline at 5 weeks of age in AR2 mice and rapidly fell to low levels during the initial 5–6 months, remaining stable until 18 months of age. Control mice exhibited full performance (180 s) until ~12 months of age, followed by slightly lower performance (>164.5 ± 6.4 s) until 24 months. *B*, Grip strength measured declined with kinetics similar to those of rotarod performance. In *A* and *B*, the scores obtained for the AR2 mice (mean ± SEM; $n = 28$) are indicated as percentage performance of control mice ($n = 15$). *C*, AR2 mice exhibited slightly lower body weight than controls ($p > 0.05$). *D*, AR2 mice ($n = 33$) had long lifespans, but the rate of death increased after month 18. The median ± SEM survival was 81.5 ± 16.4 weeks for AR2 mice compared with 105.1 ± 13.5 weeks for control mice ($p = 0.0262$, log-rank analysis).

(Fig. 3*A*), when the Cre expression reached the maximum level (~50% of motor neurons) (Misawa et al., 2003). Their rotarod performance rapidly declined during the initial 5–6 months of life, followed by stable performance until about 18 months of age (Fig. 3*A*). Control mice exhibited full performance (180 s) until ~12 months of age, followed by slightly lower performance (>164.5 ± 6.4 s) until 24 months. Grip strength declined with kinetics similar to those of rotarod performance (Fig. 3*B*). The AR2 mice had slightly lower body weight than the controls (Fig. 3*C*) and were relatively long-lived (81.5 ± 16.4 weeks; mean ± SEM), although not as long as control mice (105.1 ± 13.5 weeks; $p = 0.0262$, log-rank analysis) (Fig. 3*D*).

Pathological alterations in the spinal cords and muscles
Immunohistochemical examination demonstrated that all the AHCs in the spinal cord that were immunoreactive to anti-phosphorylated neurofilament antibodies (SMI-32) showed intense ADAR2 immunoreactivity in their nuclei in control mice, whereas a fraction of these cells was devoid of ADAR2 immuno-reactivity in AR2 mice (Fig. 1*E*) (supplemental Fig. S2*B*, available at www.jneurosci.org as supplemental material). There were a number of degenerating AHCs with cytoplasmic vacuoles (Fig. 4*A*) and darkly stained degenerating axons in the ventral roots (Fig. 4*B*). The number of AHCs in AR2 mice markedly decreased between 1 and 2 months of age and then slowly decreased beyond 1 year of age (Fig. 4*C*). The number of ADAR2-positive AHCs in the AR2 mice decreased from 83 to 54% of the number of total AHCs in the age-matched control littermates between 1 and 2 months of age. The rapid reduction in the proportion of ADAR2-positive AHCs during this period is likely attributable to the Cre-

dependent recombination of the floxed ADAR2 alleles, because the number of Cre-expressing AHCs in VAChT–Cre-.Fast mice increases developmentally until 5 weeks of age (Misawa et al., 2003). After 2 months of age, the number of ADAR2-positive AHCs did not change over the course of more than 1 year, whereas that of total AHCs decreased from 80 to 54% of the number of AHCs in the age-matched control mice (Fig. 4*C*) (Table 1). Consistent with the Cre-dependent recombination, the proportion of ADAR2-lacking AHCs in AR2 mice is in accordance with that of Cre-expressing AHCs presented in the original study of VAChT–Cre mice (Misawa et al., 2003). Concomitant with AHC degeneration, the number of myelinated axons in the ventral roots was significantly decreased (Table 1).

The kinetics of neuronal loss (Fig. 4*C*) were consistent with the kinetics of progressive motor-selective behavioral deficits (Fig. 3*A,B*). The long survival with hypoactivity beyond 6 months of age indicates that the remaining ADAR2-expressing neurons functioned normally during the remainder of life. The high rate of death after 18 months may reflect the failure of the remaining AHCs to compensate for an age-related decline in skeletal muscle power, including a decline in respiratory muscle strength.

We also examined denervation of skeletal muscles. Electromyography performed on AR2 mice at 12 months of age revealed fibrillation potentials and fasciculations, which are common findings in ALS, indicative of muscle fiber denervation and motor unit degeneration and regeneration (Fig. 4*D*). We observed characteristics of denervation, including muscle fiber atrophy, centrally placed nuclei, and pyknotic nuclear clumps in the skeletal muscles of AR2 mice (Fig. 4*E*). Some neuromuscular junctions (NMJs) were not innervated and other NMJs were innervated by ramified axons that innervated more than one NMJ in AR2 mice, indicating reinnervated NMJs (Fig. 4*F*). In contrast, in control mice, all the NMJs were innervated by a single axon. The proportion of denervated NMJs decreased, whereas reinnervated NMJs increased with age in AR2 mice (Fig. 4*F*). In addition, proliferation of activated astrocytes with increased GFAP immunoreactivity and of MAC2-positive activated microglial cells was detected in the anterior horns of AR2 mice (Fig. 4*G,H*). These results suggest that degeneration of ADAR2-lacking AHCs induced degeneration of their axon terminals, and then denervated NMJs were reinnervated by collaterally sprouted axons of ADAR2-expressing AHCs after longer survival.

Neurons in the motor nuclei of cranial nerves
The numbers of large neurons in facial and hypoglossal nerve nuclei in AR2 mice were significantly smaller than those in control mice at 12 months of age, whereas the numbers of neurons in nuclei of oculomotor nerves were not decreased (Table 1). Conversely, GluR2 Q/R site editing was significantly decreased both the in oculomotor nerve nuclei (the efficiency of GluR2 Q/R site

editing, mean ± SEM: for AR2 mice, 89.7 ± 5.8%, $n = 3$; for control mice, 100%, $n = 3$, $p = 0.0048$) and in the facial nerve nuclei (for AR2 mice, 82.6 ± 9.1%, $n = 3$; for control mice, 99.2 ± 0.2%, $n = 3$, $p = 0.0017$) of AR2 mice at 12 months of age. These results indicate that ADAR2-lacking motor neurons do not always undergo cell death, and some motor neurons, including those in the oculomotor nerve nucleus, are relatively resistant to cell death mediated by deficient ADAR2. Indeed, motor neurons innervating extraocular muscles are much less vulnerable than those innervating bulbar and limb muscles in ALS patients (Lowe and Leigh, 2002).

GluR-B^R alleles prevent motor neuron death in AR2 mice

To investigate by genetic means the role of RNA editing at the GluR2 Q/R site in the death of motor neurons, we exchanged the endogenous *GluR2* alleles in AR2 mice with GluR-B^R alleles (Kask et al., 1998), which directly encode Q/R site-edited GluR2, thus circumventing the requirement for ADAR2-mediated RNA editing. AR2/GluR-$B^{R/R}$ mice were obtained by *ADAR2*$^{flox/+}$/VAChT–Cre.Fast/GluR-$B^{R/+}$ mice intercrosses to generate *ADAR2*$^{flox/flox}$/ VAChT–Cre.Fast/GluR-$B^{R/R}$ (AR2/GluR-$B^{R/R}$) mice (see Materials and Methods).

←—

These findings were observed in two other AR2 mice examined but never in control mice (Ctl; $n = 2$). *E*, Calf muscles from a wild-type mouse (left) and an AR2 mouse (middle and right) at 12 months of age. Characteristics of denervated muscles, including muscle fiber atrophy (white arrow), centrally placed nuclei, and pyknotic nuclear clumps (white arrowhead) are observed in the AR2 mouse. Hematoxylin and eosin. Scale bar, 60 μm. *F*, NMJs and distal axons. Quadriceps muscles from a wild-type mouse (Ctl; left) and an AR2 mouse (AR2; middle and right) at 12 months of age are stained with tetramethyl-rhodamine–bungarotoxin (BTX) (red) and immunostained concomitantly with anti-synaptophysin and neurofilament (SYN/NF) antibodies (green). Endplates (red) were counted as "innervated" if they were merged with axon terminals (merge; yellow). Each endplate is innervated by a thick axon terminal in the Ctl mouse. In AR2 mice, in addition to the normally innervated NMJs, some NMJs were innervated by axons that simultaneously innervate more than one NMJ (reinnervated NMJs; middle), and other NMJs were devoid of axon terminals (denervated NMJs; right). More than 50 NMJs were counted in each animal in the control group and groups of AR2 mice at 4 and 12 months of age ($n = 3$ in each group). Proportions of denervated NMJs and reinnervated NMJs among total NMJs in each group are indicated as mean ± SD (percentage). Scale bar, 25 μm. *G, H*, Immunohistochemistry in the anterior horn (C5). There was a time-dependent increase in GFAP immunoreactivity (*G*) and an increase in MAC2 immunoreactivity maximal at 6 months of age (*H*) in the spinal anterior horn of AR2 mice. m, Months of age; inset, activated astroglia. Scale bars: *G*, 100 μm; insets and *H*, 50 μm.
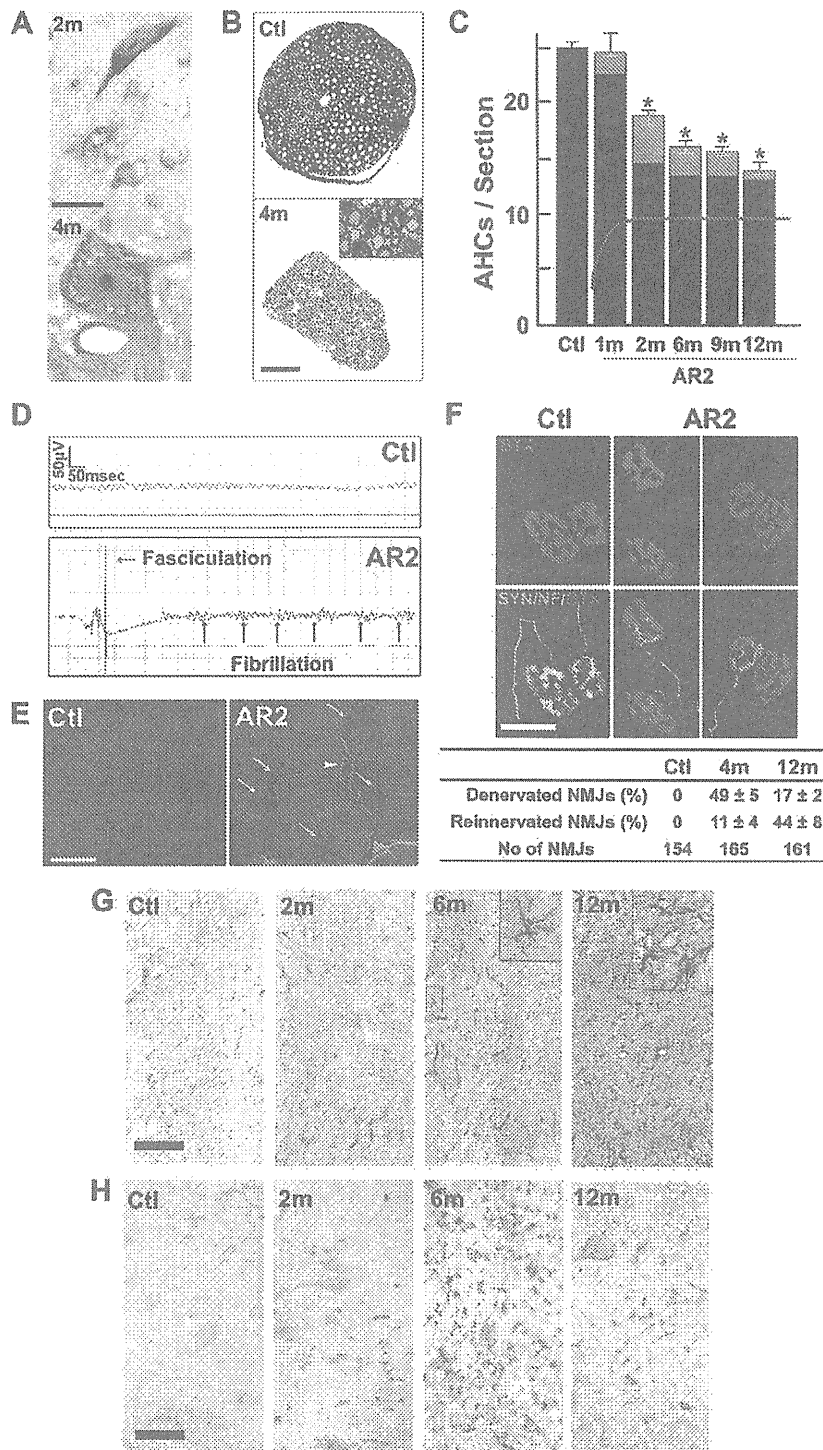
Figure 4. Loss of ADAR2-deficient motor neurons. *A*, Degenerating AHCs in AR2 mice at 2 months (2m; Nissl staining) and 4 months (4m; toluidine blue staining, 1 μm section) of age. Scale bar: 2m, 25 μm; 4m, 12.5 μm. *B*, Ventral root (L5) of control (Ctl) and AR2 mice at 4 months of age (4m). Inset, Magnified view of degenerating axons. Scale bar: 100 μm; inset, 20 μm. *C*, Numbers of AHCs showing ADAR2 immunoreactivity (black columns) and lacking this immunoreactivity (gray columns) (mean ± SEM) in AR2 mice at different ages (1m, 2m, 6m, 9m, 12m). In AR2 mice, Cre expression is developmentally regulated (orange line), and ~50% of motor neurons express Cre by 5 weeks of age, with recombination of the *ADAR2* gene in ~10% of AHCs at 1 month of age and 40–45% of AHCs after 2 months of age (orange line). The number of ADAR2-lacking AHCs significantly decreased in AR2 mice after 2 months of age as a result of Cre-dependent knock-out of ADAR2 (*$p < 0.01$, repeated-measures ANOVA). The number of AHCs in the control mice did not change at different ages, and all the AHCs in controls showed ADAR2 immunoreactivity. *D*, Electrophysiological examination in AR2 mice. Electromyography from an AR2 mouse at 12 months of age showing fibrillations and fasciculations, common findings in ALS indicative of muscle fiber denervation and motor unit degeneration and regeneration.